Journal of Asian Earth Sciences 188 (2020) 104111

Contents lists available at ScienceDirect

Journal of Asian Earth Sciences

journal homepage: www.elsevier.com/locate/jseaes

Effects of sediment addition on magma generation from oceanic crust in a post-collisional extensional setting: Constraints from partial melting experiments on mudstone–amphibolite/basalt at 1.0 and 1.5 GPa

Chunjuan Zang[a,b,c], Hongfeng Tang[b,*], Mingliang Wang[a,b,c]

[a] School of Resource and Civil Engineering, Suzhou University, Suzhou, Anhui 234000, PR China
[b] Key laboratory of High Temperature & High Pressure Study of the Earth's Interior, Institute of Geochemistry, Chinese Academy of Science, Guiyang 550081, PR China
[c] Key Laboratory of Mine Water Resource Utilization of Anhui Higher Education Institute, Suzhou University, Suzhou, Anhui 234000, PR China

ARTICLE INFO

Keywords:
Post-collisional extension
Sediment
Partial melting
Oceanic basalt
East Junggar

ABSTRACT

To assess the effects of sediment addition on magma generation from oceanic crust during post-collisional extension, we conducted partial melting experiments on amphibolite–mudstone (90 and 10 wt%, respectively) and basalt–mudstone (90 and 10 wt%, respectively) mixtures at 850–1000 °C and 1.0 and 1.5 GPa. In the experimental products, partial melt coexists with Amp ± Pl ± Grt ± Cpx at 1.0 GPa and Grt ± Cpx ± Amp at 1.5 GPa. Given the high water content of the sediment (> 5 wt%), the partial melts are hydrous even without the addition of water. Compared with previous partial melting experiments on (meta)basalts, our experiments yield similar phase assemblages (Amp ± Pl ± Grt ± Cpx) but different *P–T* conditions for mineral stabilities. Sediment addition makes the residual minerals (Amp, Pl, and Cpx) more fusible and the crystallization of new minerals (Grt and Cpx) more difficult, thereby producing a high proportion of melt (> 50 vol%) at > 900 °C. In the case of high-degree partial melting, the melt is enriched in Al_2O_3 and depleted in SiO_2. Sediment addition enriches the partial melts in Rb, Th, U, and light rare earth elements, and results in high Y contents, low Sr/Y and very low La_N/Yb_N ratios. These effects are apparent in a natural example from east Junggar in northwest China, where granitoids have major and trace element features comparable with those of partial melts from the amphibolite–sediment mixture at 1.5 GPa. This indicates that sediment addition has a significant effect on magma generation from oceanic crust in a post-collisional extensional setting.

1. Introduction

Oceanic crust is generated by partial melting of mantle at a mid-ocean ridge and is returned to the mantle at a subduction zone. This cycle plays an important role in modifying the geochemistry of Earth reservoirs (Allègre, 1988; Anderson, 2007; Frisch et al., 2011; Zheng et al., 2015). Furthermore, subducted oceanic crust partially melts at convergent plate margins, such as in young subduction and/or collisional zones or in post-collisional extensional settings (Dai et al., 2017; Huene and Scholl, 1991; Maury et al., 1996; Peacock et al., 1994; Rapp and Watson, 1995; Taylor and Mclennan, 1995). Subducted sediments are also involved in the partial melting process, which can be detected via the geochemical and isotopic characteristics of magma (Hermann and Spandler, 2008; Hu et al., 2017; Johnson and Plank, 2000; Tera et al., 1986). Most sediment is scraped off the oceanic crust before subduction into the mantle, and the contribution of sediment during partial melting is small compared with the contribution of subducted oceanic basalt (Zheng et al., 2015 and references therein). The sediment contribution is between 10 and 30 wt% (Niu, 2013). The aim of the present study was to experimentally establish how such small amounts of sediment affect the partial melt generated in a post-collisional extensional setting.

We also compare our experimental results with the compositions of granitoids in east Junggar, northwestern China (Fig. 1) where numerous post-collisional calc-alkaline granitoids (I-type granite, including monzogranite and granodiorite) are spatially associated with the Kalamali ophiolite (Zhu et al., 2006), which are considered to be related to slab subduction (Coleman, 2012; Dilek and Furnes, 2014; Dilek and Newcomb, 2003). These granitoids have relatively high εNd (t) and εHf(t) values (Chen and Jahn, 2004; Gan et al., 2010; Han et al., 1997; Su, 2007; Tang et al., 2008; Xue et al., 2010; Yang et al., 2011), indicating a close relationship with the mantle. The U–Pb ages of the granitoids are later than the emplacement age of the Kalamali ophiolite (Gan et al., 2010; Han et al., 2006; Tian et al., 2016), and a subducted

* Corresponding author.
E-mail address: tanghongfeng@vip.gyig.ac.cn (H. Tang).

https://doi.org/10.1016/j.jseaes.2019.104111
Received 21 August 2018; Received in revised form 19 October 2019; Accepted 24 October 2019
Available online 25 October 2019
1367-9120/

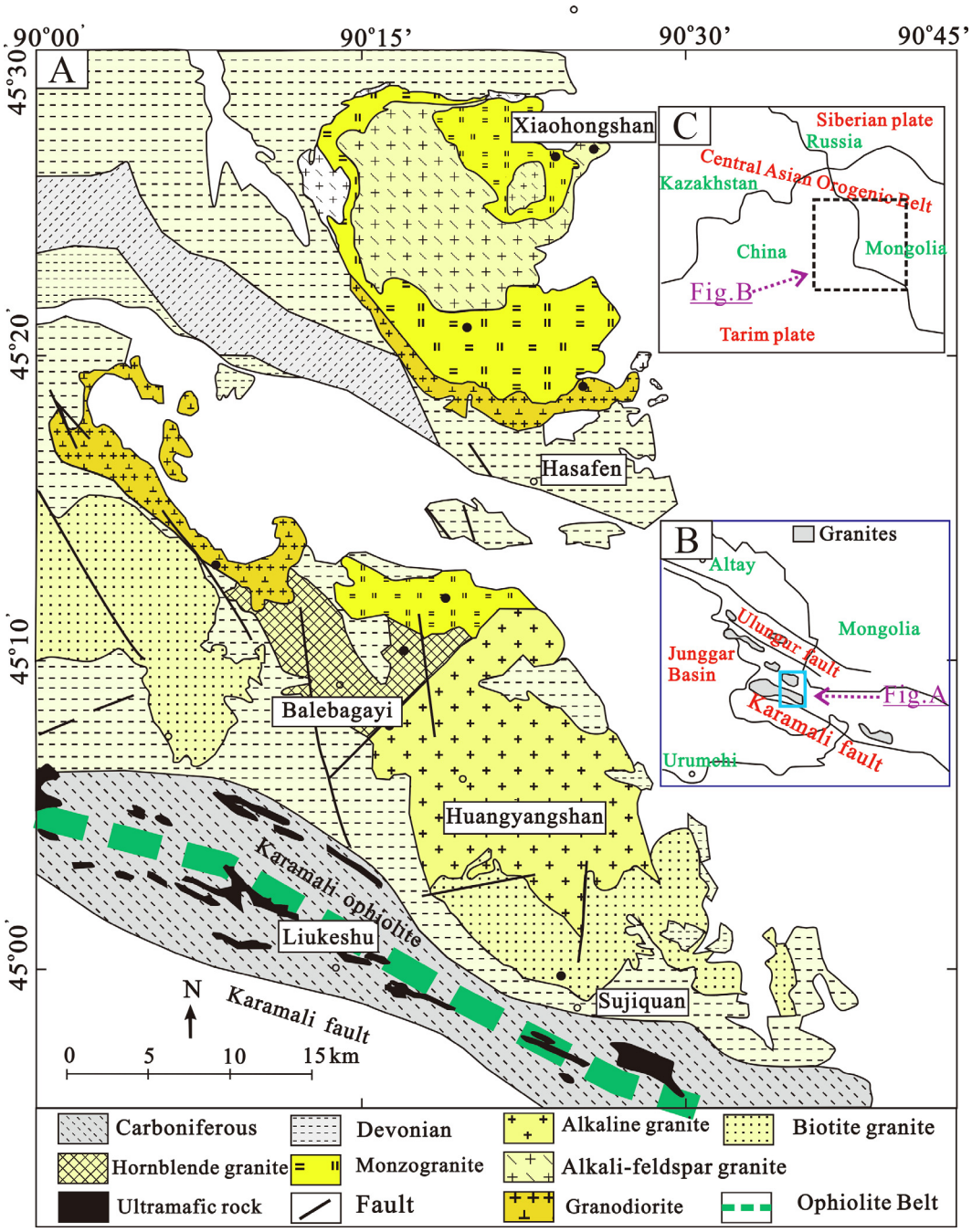

Fig. 1. Geological sketch map of granitic intrusives in east Junggar. (A) Major tectonic divisions of Central Asian Orogenic Belt. (B) Tectonic divisions of east Junggar. Both A and B after Chen and Jahn (2004). (C) Detailed spatial distribution of granitic intrusive (after Su (2007)). The calc-alkaline granitic intrusive include monzogranite and granodiorite located nearby the karamali ophiolite.

slab was temporally and spatially associated with the granitoids (Han et al., 2006; Xue et al., 2010). As such, the intrusions were likely generated by partial melting of subducted oceanic crust during post-collisional extension, with or without the involvement of sediments (Gan et al., 2010; Han et al., 1997; Tang et al., 2008). Given that it is difficult to determine whether sediment was involved in magma generation via field observations alone, the effect of sediment addition can be assessed by comparing the granite geochemistry with that of melts produced in high-pressure partial melting experiments of basalt ± sediment.

Numerous partial melting experiments have been conducted on basalts and similar rocks (amphibolites, gabbros), yielding a variety of intermediate to silicic melts (summarized in Fig. 2; results from Beard and Lofgren, 1991; Koepke et al., 2004; Qian and Hermann, 2013; Rapp and Watson, 1995; Rapp et al., 1991; Rushmer, 1991; Sen and Dunn, 1994; Sisson et al., 2005; Takahahshi et al., 1998; Xiong et al., 2005, 2006; Yaxley and Green, 1998). Beard and Lofgren (1991) established that low-K silicic rocks in arc settings are generated by dehydration melting of the subducting slab, and Rushmer (1991) and Sisson et al. (2005) showed that the mafic rocks in slab residues can be granite sources, even under water-absent conditions. Experimental studies indicate that trondhjemite–tonalite–granodiorite (TTG) rocks originate by partial melting of a subducting slab at pressures of > 0.8 GPa, with garnet as a residual phase in the source (Laurie and Stevens, 2012; Qian and Hermann, 2013; Rapp and Watson, 1995; Rapp et al., 1991; Sen and Dunn, 1994). This is also the case for adakites, which have similar

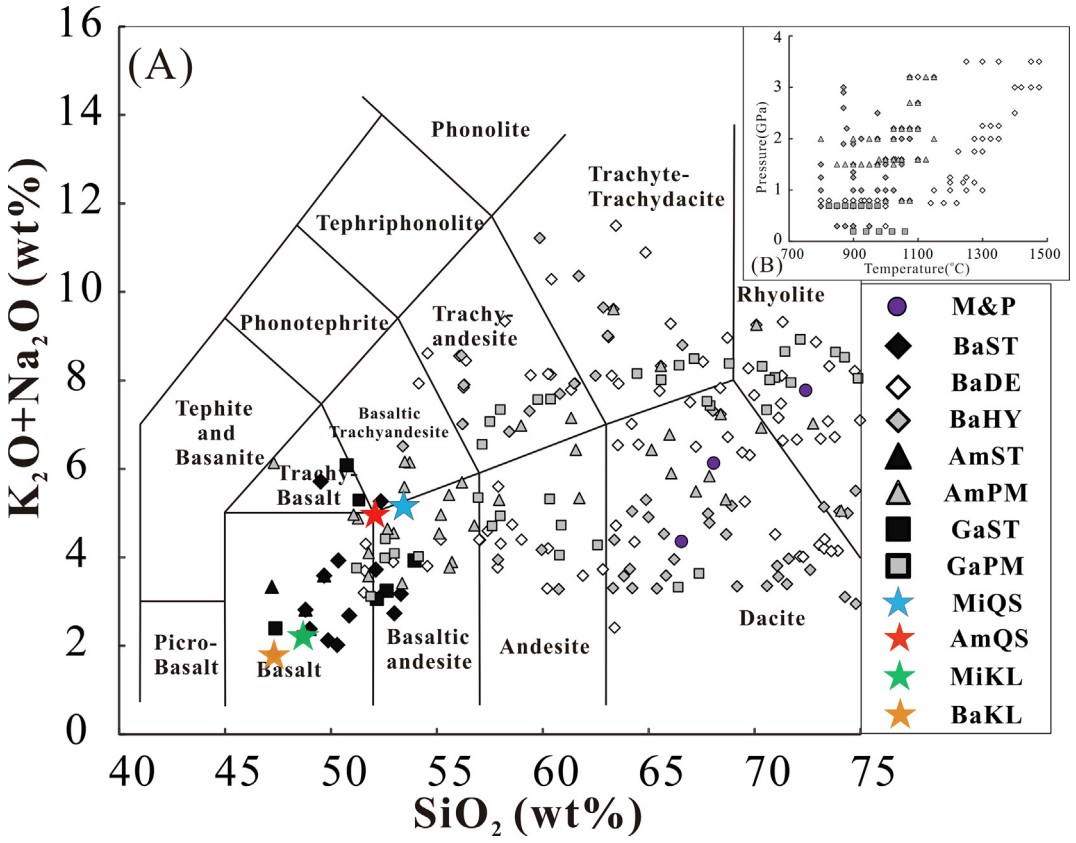

Fig. 2. Compositions of starting materials and run product-melts in partial melting experiments on basites. (A) Total alkali versus silica (TAS) variation diagram, classification and nomenclature of TAS diagram follow Maitre (1989). (B) Temperature and pressure rang of partial melting experiments on basic rocks. M&P, Melts from layered basalt-mudstone mixture in Mccarthy and Patiño Douce (1997); BaST, Starting material of basalts; BaDE, Melts generate in dehydration melting experiments on basalts; BaHY, Melts generate in partial melting of hydrous basalt (Beard and Lofgren, 1991; Qian and Hermann, 2013; Rapp and Watson, 1995; Rapp et al., 1991; Rushmer, 1991; Sisson et al., 2005; Takahahshi et al., 1998; Xiong et al., 2005, 2006; Yaxley and Green, 1998). AmST, Starting material of amphibolites; AmPM Melts generate in partial melting experiments onamphibolites (Rapp and Watson, 1995; Sen and Dunn, 1994). GaST, Starting material of gabbros; GaPM, Melts generate in partial melting experiments on gabbros (Koepke et al., 2004; Sisson et al., 2005). MiQS, Staring amphibolite-mudstone mixture used in this study; AmQS, Starting material amphibolite QS08-1; MiKL, Staring basalt-mudstone mixture used in this study; BaKL, Starting material basalt KL24.

geochemical characteristics to TTGs. Xiong et al. (2005, 2006) reported that rutile is another key residual mineral in the source region of TTG (or adakitic) rocks. Mccarthy and Patiño Douce (1997) under took partial melting experiments on layered basalt–sediment mixtures and demonstrated that sediment addition yields compositionally distinct partial melts from those obtained when melting basalt alone (Fig. 2).

The experiments described above are important for a number of reasons. Firstly, the experimental data for partial melting of basalt provide a baseline for assessing the effects of the addition of small amounts of sediment. Secondly, the results of Mccarthy and Patiño Douce (1997) confirm that sediment addition has a strong effect on the phase relations and melt compositions of partial melting products. However, the starting material used in Mccarthy and Patiño Douce (1997) contained unrealistically large amounts of sediment. In the present study, two basalt/amphibolite–mudstone mixtures containing 10 wt% mudstone were used as the starting materials, allowing us to investigate the effects of adding a small amount of sediment. In the following sections, we first describe the starting materials and analytical methods. We then compare in detail the partial melts from these mixtures with those from (meta)basalts under similar P–T conditions. Finally, we highlight a natural example of granite from east Junggar, northwest China, which verifies the strong effects of the addition of a small amount of sediment during the partial melting of subducted oceanic basalt in a post-collisional extensional setting.

2. Experimental and analytical methods

2.1. Starting materials

The amphibolite (QS08-1), basalt (KL24), and mudstone (SJ41) samples were all collected from the inner Kalamali ophiolite. The chemical compositions and mineral contents of these samples are listed in Table 1. The amphibolite (QS08-1) contains 60 vol% amphibole (Amp), 38 vol% plagioclase (Pl), and trace amounts of ilmenite (trace), which are representative of local metamorphosed oceanic basalts from the top of an oceanic crustal section. The oceanic basalt was metamorphosed during seawater–rock interactions after eruption, has a high Na_2O content (up to 4.75 wt%), and a rare earth element (REE) pattern consistent with a normal mid-ocean ridge basalt (N-MORB) composition. The unaltered basalt sample (KL24), a typical MORB from the inner Kalamali ophiolite (Liu et al., 2007), contains ~40 vol% clinopyroxene (Cpx), 25 vol% Pl, and glass. The mudstone sample is terrigenous sediment that was collected from near the amphibolite sample. The mudstone contains quartz and clay minerals. There are no carbonates in these three starting materials, and thus the loss-on-ignition (LOI) values are due mainly to H_2O.

A mixture of 90 wt% basalt/amphibolite and 10 wt% mudstone was chosen for the starting material, as guided by a Hf isotopic study of the local granitoid that indicated 5–10 wt% of terrigenous sediment was added to the magma source (Gan et al., 2010). This figure is in the lower part of the range (10–30 wt%) for the proportion of sediment in subducted oceanic crust, as estimated by Niu (2013). The three starting

Table 1
The major and trace element compositions of the starting materials.

sample number	Amphibolite (QS08-1) whole rock	Amp in QS08-1 (60%)	Pl in QS08-1 (38%)	Basalt KL24 whole rock[b]	Cpx in Kl24 (40%)	Pl in Kl24 (25%)	Mudstone SJ41 Whole rock	Starting Mixture QS[a]	Starting Mixture KL[a]
Major elements(wt.%)									
SiO_2	51.99	44.15	69.74	45.50	52.27	67.14	58.65	52.33	46.82
TiO_2	1.36	2.22	–	0.91	0.49	0.01	0.83	1.30	0.90
Al_2O_3	14.44	8.93	20.02	14.85	3.38	19.29	18.18	14.72	15.18
Fe_2O_3	12.99	–	–	9.03	–	–	8.16	12.43	8.94
FeO	–	19.62	0.09	–	5.24	0.16	–	–	–
MnO	0.21	0.41	0.01	0.14	0.20	0.04	0.08	0.20	0.13
MgO	5.09	9.77	–	9.35	18.12	0.02	2.29	4.78	8.64
CaO	7.66	9.94	0.34	14.81	20.10	0.17	1.21	6.97	13.45
Na_2O	4.75	2.32	10.50	1.70	0.19	11.26	2.71	4.52	1.80
K_2O	0.33	0.21	0.04	0.02	0.02	0.08	2.70	0.56	0.29
P_2O_5	0.10	0.05	0.04	0.06	0.02	0.03	0.17	0.11	0.07
LOI	1.71	–	–	3.46	–	–	5.66	2.09	3.68
Total	100.63	97.61	100.79	99.85	100.03	98.19	100.64	100.00	99.93
Trace elements (ppm)									
Sc	35.4	–	–	36	–	–	19.7	33.8	34.4
V	284	–	–	260	–	–	165	272	251
Cr	10.7	–	–	110	–	–	63.0	15.9	105
Co	36.4	–	–	35.3	–	–	14.5	34.2	33.2
Ni	14.2	–	–	54.3	–	–	29.1	15.7	51.8
Cu	56.4	–	–	75.0	–	–	81.0	58.9	75.6
Zn	99.9	–	–	75.1	–	–	99.7	99.9	77.6
Ga	17.8	–	–	–	–	–	20.0	18.0	–
Rb	3.89	–	–	0.3	–	–	73.9	10.9	7.66
Sr	563	–	–	67.4	–	–	271	534	87.8
Y	28.2	–	–	19.8	–	–	22.4	27.6	20.1
Zr	73.3	–	–	0.89	–	–	154	81.4	16.2
Nb	1.33	–	–	–	–	–	6.50	1.85	–
Sn	0.696	–	–	0.36	–	–	1.73	0.80	0.50
Cs	0.114	–	–	9.00	–	–	7.75	0.88	8.88
Ba	193	–	–	2.45	–	–	416	215	43.81
La	4.01	–	–	6.89	–	–	18.7	5.48	8.07
Ce	11.0	–	–	1.26	–	–	39.3	13.8	5.06
Pr	1.82	–	–	6.27	–	–	5.03	2.14	6.15
Nd	9.58	–	–	2.18	–	–	21.8	10.8	4.14
Sm	3.31	–	–	0.81	–	–	4.46	3.43	1.18
Eu	1.22	–	–	2.96	–	–	1.13	1.21	2.78
Gd	4.25	–	–	0.58	–	–	4.39	4.26	0.96
Tb	0.755	–	–	3.77	–	–	0.68	0.75	3.46
Dy	4.93	–	–	0.84	–	–	4.13	4.85	1.17
Ho	1.14	–	–	2.36	–	–	0.90	1.12	2.21
Er	3.26	–	–	0.34	–	–	2.74	3.21	0.58
Tm	0.463	–	–	2.27	–	–	0.42	0.46	2.09
Yb	3.10	–	–	0.36	–	–	2.85	3.08	0.61
Lu	0.456	–	–	1.73	–	–	0.45	0.46	1.60
Hf	2.16	–	–	0.07	–	–	4.14	2.36	0.48
Ta	0.101	–	–	–	–	–	0.43	0.13	–
Pb	0.620	–	–	0.17	–	–	10.2	1.58	1.17
Th	0.344	–	–	0.07	–	–	5.08	0.82	0.57
U	0.275	–	–	0.89	–	–	1.61	0.41	0.96

[a] Theoretical calculating value.
[b] Data from Liu et al. (2007).

materials were ultrasonically cleaned in distilled water and alcohol, and then manually crushed to powder with a grain size of ~120 meshes (125 μm). The amphibolite and basalt powders were then mixed with mudstone powder to produce two mixtures (QS and KL, respectively). The two mixtures were placed in an agate mortar and ground for > 3 h to ensure that the particle size was ≤10 μm.

2.2. Experimental procedures

The furnace assembly used in our experiments is similar to those of Wang and Tang (2013) and Wang et al. (2019) (Fig. 3). Graphite-lined Pt capsules (d = 3.5 mm, h = 3.0 ± 0.1 mm) with graphite lids on the top and bottom were used to minimize Fe loss. The starting mixtures were pressed into tablets and placed in the inner graphite capsules. Ultrapure water was added to the samples with a micropipette (Hanlin 0.1–2.5 μL, uncertainty at 1 μL of ± 3%) in amounts from 0% to 4%; the error in the water content was less than ± 5%. The Pt capsules were sealed by welding and carefully examined for leaks using binocular microscopy and water immersion. The capsules were then placed in an oven at 105 °C for 24 h to dry. If the mass of a capsule remained unchanged before and after drying, the capsule was regarded as being suitable for further experimental work. Each sealed capsule was surrounded by an Al_2O_3 sleeve and placed into the middle of a graphite heater. The space above and below each capsule was filled with pyrophyllite cylinders that had been fired at 800 °C. The graphite heating tube was finally placed into a pyrophyllite cube (32 × 32 × 32 mm), which had also been fired at 800 °C.

The experiments were conducted in a DS6*600t six-anvil apparatus equipped at the Key Laboratory for High Temperature and High Pressure Study of the Earth's Interior, Institute of Geochemistry,

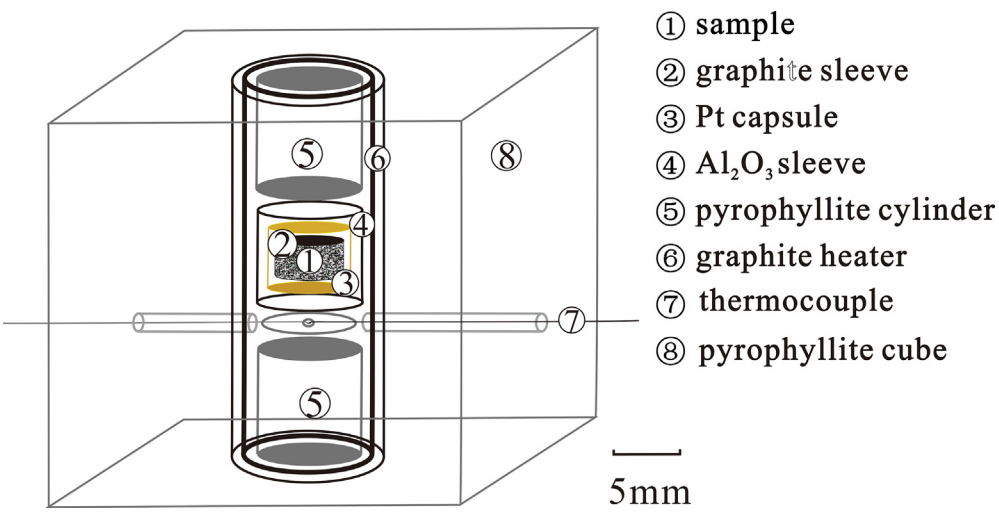

Fig. 3. Sketch map of sample assemblage.

Table 2
Summary of experimental conditions.

Run No.	P (GPa)	T (°C)	Water (wt.%)	Time (h)	Phase assemblage	Melt proportion (vol.%)
Partial melting of Mixture QS						
TD06	1.0	850	2	96	Melt + Amp + Pl + Ilm	11
TD10	1.0	850	4	96	Melt + Amp + Pl + Ilm	16
TD05	1.0	900	2	96	Melt + Cpx + AmpPl + Ilm	19
TD14	1.0	925	2	120	Melt + Amp + Grt + Pl	60
TD13	1.0	950	0	96	Melt + Cpx	82
TD12	1.0	1000	0	96	Melt + Cpx	98
TD03	1.0	1000	2	96	Melt + Cpx	95
TD07	1.0	1000	4	96	Melt + Cpx(?)	99
TD24	1.5	900	2	120	Melt + Amp + Grt	57
TD25	1.5	900	4	120	Melt + Amp + Grt	54
TD22	1.5	925	2	120	Melt + Cpx + Grt	64
TD23	1.5	925	4	120	Melt + Cpx + Grt	66
TD19	1.5	950	0	96	Melt + Cpx + Grt	72
TD20	1.5	950	2	96	Melt + Cpx + Grt	69
TD21	1.5	950	4	96	Melt + Cpx + Grt	68
TD16	1.5	975	0	96	Melt + Cpx + Grt	72
TD17	1.5	975	2	96	Melt + Cpx + Grt	70
TD18	1.5	975	4	96	Melt + Cpx + Grt	71
Partial melting of Mixture KL						
XD09	1.5	900	4	120	Melt + Cpx + Amp + Grt	31
XD07	1.5	925	4	120	Melt + Cpx + Grt	37
XD04	1.5	950	0	96	Melt + Cpx + Grt	52
XD06	1.5	950	4	96	Melt + Cpx + Grt	55
XD01	1.5	975	0	96	Melt + Cpx + Grt	59
XD02	1.5	975	2	96	Melt + Cpx + Grt	60
XD03	1.5	975	4	96	Melt + Cpx + Grt	61

Phase abbreviation: Amp-amphibole, Cpx-clinopyxene, Grt-garnet, Ilm-ilmenite Opx-orthopyroxene, Pl-plagioclase.

Chinese Academy of Sciences, Guiyang, China. The pressure was calibrated using the Bi phase transitions at room temperature and the Au melting curve at 0.6–6.0 GPa (Fu and Zhu, 1986). We subsequently confirmed this calibration using the KCl melting curve of Tingle et al. (1993). For each run, the pressure was first increased to the target value, and the temperature was then increased to the target value in three steps at constant pressure. The experiment was considered to have begun (in terms of time elapsed) once the temperature reached the target value. After design time (96 h or 120 h), the sample was quenched to < 80 °C over 90 s by turning the power off and decompressing the apparatus. The temperature was measured with a NiCr–NiSi thermocouple and controlled to ± 5 °C, while the pressure was estimated from the piston cylinder pressure and controlled to ± 0.1 GPa. After decompression, the sample was carefully removed from the capsule, mounted in epoxy, and polished for observation under optical microscopy and for electron microprobe analysis.

2.3. Analytical methods

The major and trace element analyses of the starting materials were carried out in the State Key Laboratory of Ore Deposit Geochemistry, Institute of Geochemistry, Chinese Academy of Sciences, Guiyang, China. The major elements in the starting materials were measured by X-ray fluorescence spectrometry (XRF; PW4400, Axios) and the trace elements by inductively coupled plasma–mass spectrometry (ICP–MS), following the procedures of Qi et al. (2000). Analyses of standard reference materials are listed in Supplement ***S1-stands***. Back-scattered electron (BSE) images and major element compositions of the experimental products (minerals and glasses) were obtained using a JEOL JXA-8100 electron microprobe at the Key Laboratory of Mineralization and Dynamics, Chang'an University, Xi'an, China. The beam diameter used for the melt analyses was 5–10 μm, with an accelerating voltage of 15 kV and beam current of 2 nA. Detailed analytical procedures are

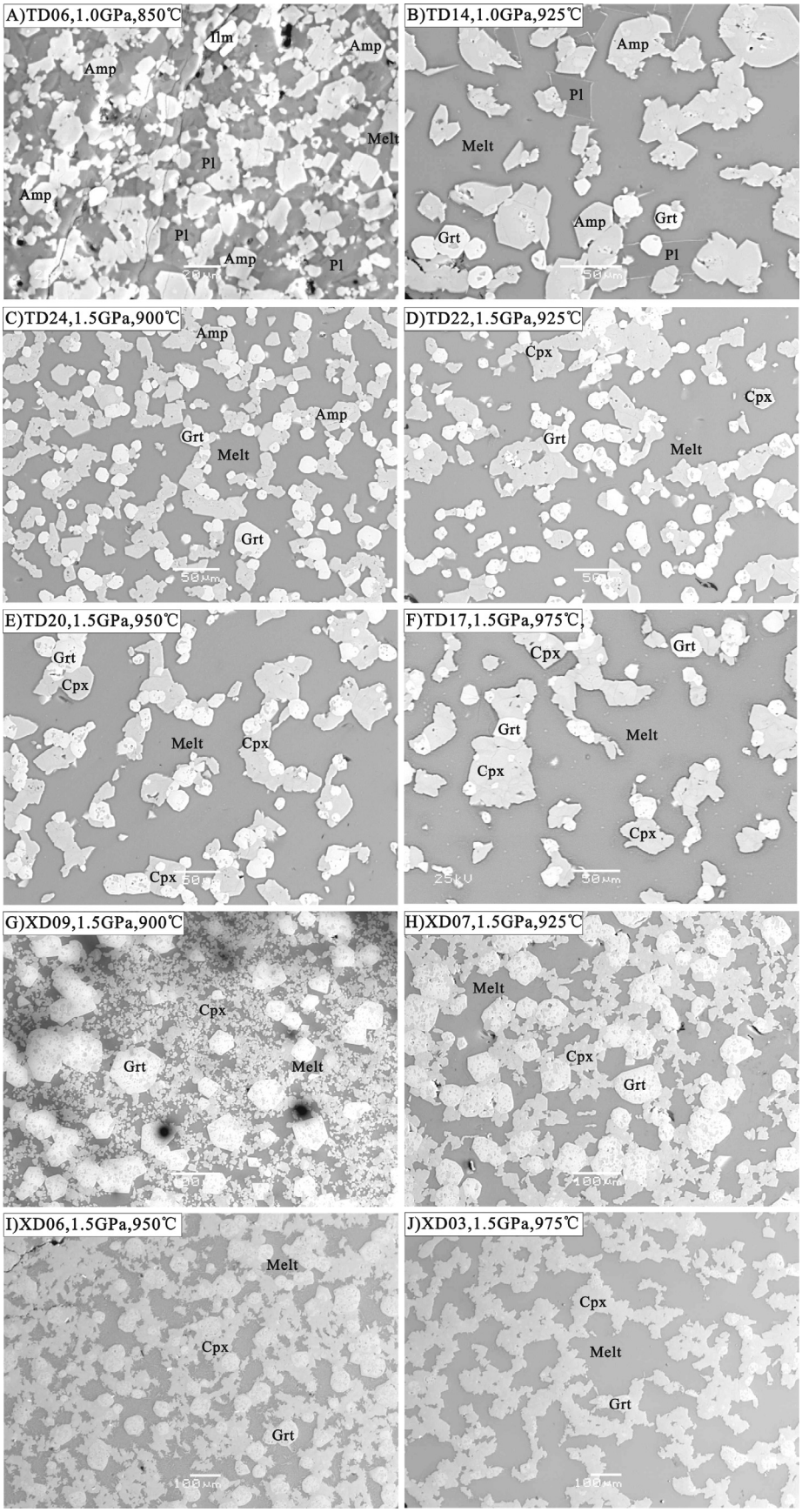

Fig. 4. Representative BSE photos of experiment products. Phase abbreviation: Amp-amphibole, Cpx-clinopyxene, Grt-garnet, Ilm-ilmenite, Opx-orthopyroxene, Pl-plagioclase.

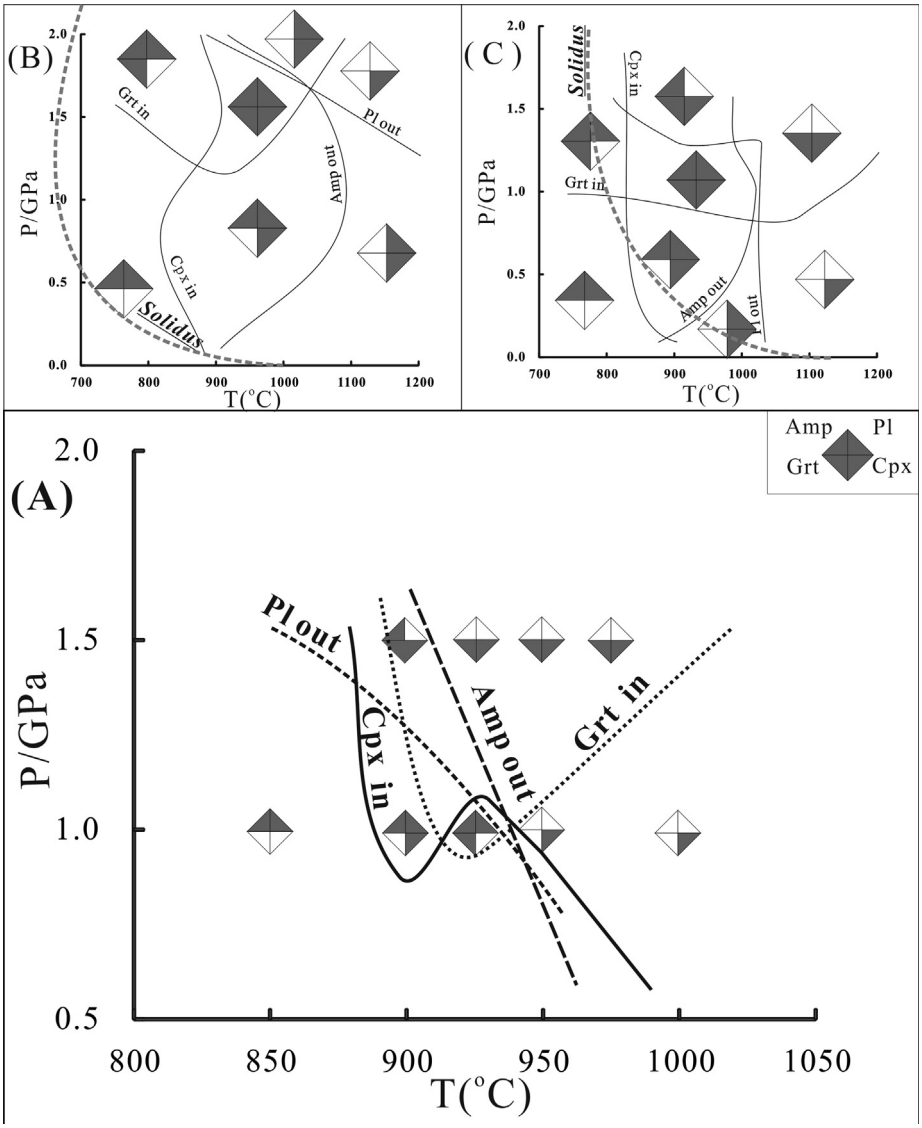

Fig. 5. Phase assemblages of the experimental runs and limits of stability of major phases. (A) Partial melting of basalt-mudstone mixture at 1.0–1.5 GPa. (B) Partial melting of hydrous basalt at below 2.0 GPa. (C) Dehydration melting experiments on basalt at below 2.0 GPa (Beard and Lofgren, 1991; Qian and Hermann, 2013; Rapp and Watson, 1995; Rapp et al., 1991; Rushmer, 1991; Sisson et al., 2005; Takahahshi et al., 1998; Xiong et al., 2005, 2006; Yaxley and Green, 1998). The solidus in (B) refers to Xiong et al. (2006), the one in (C) refers to (Sen and Dunn, 1994).

provided by Huang et al. (2007). Possible loss of Na and K during the melt analyses was assessed by analysis of a glass with a known composition. The uncertainties of the major element analyses are less than ± 5%. Trace element compositions of the partial meltswere determined by laser ablation (LA)–ICP–MS with a GeoLasProLA system coupled to an ELAN DRC-e ICP–MS at the State Key Laboratory of Ore Deposit Geochemistry, Institute of Geochemistry, Chinese Academy of Sciences, Guiyang, China. The analytical procedures and errors (less than ± 10%) were the same as reported by Liu et al. (2008), and trace element results for standard reference materials are also listed in Supplement ***S1-stands***.

3. Experimental results

The mineral assemblages and melt proportions obtained under different run conditions are listed in Table 2. Representative BSE images of experimental products are shown in Fig. 4, and phase assemblages of the experimental runs and limits of stability of the major phases are shown in Fig. 5. The melt proportions in the BSE images of the experimental products were determined by the software*Image J* and by point-counting. The maximum error of these two methods is ± 4%. The change in melt percentage with increasing temperature, as compared with previous studies, is shown in Fig. 6. The major element compositions of the partial melts are listed in Table 3, normalized to 100 wt%. The averaged original totals are also provided in the table. Trace element compositions of the partial melts from mixture QS are listed in Table 4. The major element compositions of the residual minerals from mixture QS are given in supplement ***S1-Table 6***.

3.1. Phase assemblages

In the 1.0 GPa runs, the melt proportions in the experimental products at 850 °C and 900 °C were 11–19 vol%. The melts are sporadically distributed amongst the residual minerals (Fig. 4A), coexisting with Amp and Pl, which were both in the starting QS mixture. For these runs (TD06, TD10, and TD05), the size of a small number of mineral crystals increased to 20–30 μm, whereas the size of most mineral crystals remained unchanged. For the run at 925 °C, the melt proportion increased markedly to ~60 vol% (Figs. 4B and 6) and coexists with Amp + Pl + garnet (Grt). The size of the minerals also increased

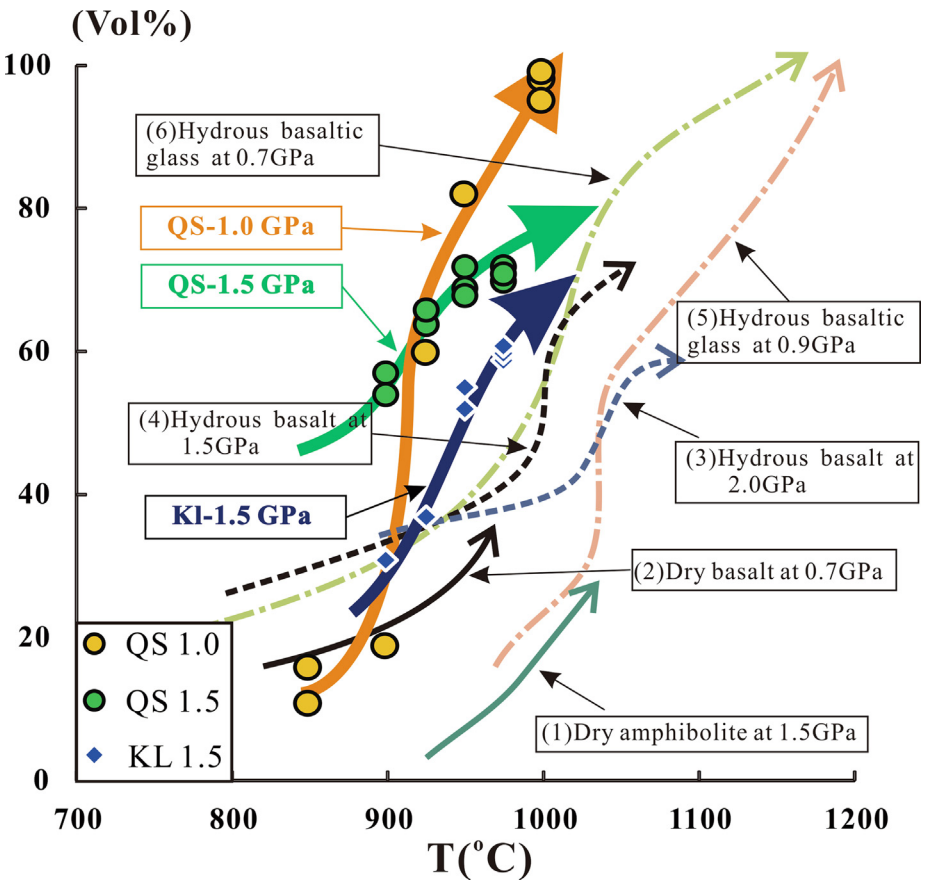

Fig. 6. Melt proportionscurves of partial melting experiment on basic rocks. (1) Dry amphibolite at 1.5 GPa from Sen and Dunn (1994); (2) Dry basalt at 0.7 GPa from Sisson et al. (2005); (3) Hydrous basalt at 2.0 GPa from Xiong et al. (2005); (4) Hydrous basalt at 1.5 GPa from Qian and Hermann (2013); (5) Hydrous basaltic basalt at 0.9 GPa from Blatter et al. (2013); (6) Hydrous basaltic basalt at 0.7 GPa from Nandedkar et al. (2014). QS 1.0, partial melts on mixture QS at 1.0 GPa in this study; QS 1.5, partial melts on mixture QS at 1.5 Pa in this study; KL 1.5, partial melts on mixture KL at 1.5 GPa in this study. A sharp increasing can be observed at 900–925 °C in this study which are distinct from other results.

noticeably: the length of the Amp crystals was ~80 μm, the diameter of Pl was ~40 μm, and the Grt grains were typically euhedral and up to 20 μm in diameter. For the runs at 950 °C and 1000 °C, the melt proportion increased to > 80 vol%, and the only mineral coexisting with the melt was Cpx, with a grain size of up to 100 μm. This reaction process can be described as follows: Amp + Pl + sediment → Melt ± Cpx.

For the runs on mixture QS at 1.5 GPa, the melt at 900 °C coexisted with Amp + Grt, the melt volume percentage was 54–57 vol% (Fig. 4C), and the diameter of Amp grains was ~30 μm, similar to the euhedral Grt in the same runs. In the runs at 925 °C, 950 °C, and 975 °C, the melt proportions were 64–72 vol% (Fig. 4D–F). In these runs, the melt coexists with Cpx + Grt and the diameter of Cpx increased with temperature from 40 to 70 μm, whereas the size of the Grt grains remained constant at ~30 μm. Grt and Cpx were not present in the starting materials, but were formed during the partial melting process. This process can be described as follows: Amp + Pl + sediment → Melt ± Cpx ± Grt.

For the run on mixture KL at 1.5 GPa, the melt at 900 °C coexists with Amp + Grt + Cpx, and produced 31 vol% melt (Fig. 4G). The diameters of Amp and Cpx grains were ~10 μm, whereas the large euhedral Grt has a diameter of 100 μm. The melts in runs at 925–975 °C all coexist with Cpx + Grt, and the melt percentages increase from 37 to 61 vol% (Figs. 4H–J and 6). The Cpx in these runs were larger than in the run at 900 °C, with diameters of 30–50 μm. The crystal size of Grt decreased with increasing temperature, from 80 μm at 925 °C (Fig. 4H) to 20 μm at 975 °C (Fig. 4J). This process can be described as follows: Cpx + Pl + sediment → Melt + Grt ± Amp.

3.2. Major and trace element compositions of the partial melts

The partial melts are homogeneous in composition. The major element compositions of the partial melts for different runs are shown in Fig. 7. SiO_2 contents (55–73 wt%) decreased with increasing run temperature, and Na_2O and K_2O contents showed similar trends, whereas TiO_2, FeO, MgO, and CaO contents increased. The effect of run pressure on the major element compositions of the partial melts is negligible, except for Al_2O_3 and Na_2O, when comparing the runs on mixture QS at 1.0 and 1.5 GPa. The partial melts at 1.5 GPa are enriched in Al_2O_3 and Na_2O compared with those at 1.0 GPa, because plagioclase, which is rich in Al_2O_3 and Na_2O (Table 1), was present at 1.0 GPa and exhausted at 1.5 GPa. The effects of the starting materials on major elements is significant, and melts of mixture QS have higher SiO_2, FeO, and Na_2O contents and lower Al_2O_3, MgO, and CaO contents as compared with melts of mixture KL at the same temperature and pressure, which is consistent with the original differences in major elements between mixtures QS and KL (Table1).

Chondrite-normalized trace element and REE patterns for the partial melts are shown in Fig. 8A and B. The partial melts have negative Nb anomalies, similar to the starting materials, and melt in runs at 850–900 °C and 1.0 GPa have a negative Ti anomaly, which might be caused by ilmenite crystallization (Fig. 4A; Table 2). Compared with the starting amphibolite composition, partial melts from the mixtures are enriched in Rb, Th, U, La, and Ce (Fig. 8A), as with the sediment in the mixture (Table 2). The REE patterns of the partial melts are enriched in light REE (Fig. 8B) and are clearly different from the flat REE patterns of the starting mixture QS and the amphibolite.

4. Discussion

4.1. Approach to equilibrium

According to previous experimental studies (Beard and Lofgren, 1991; Qian and Hermann, 2013; Sen and Dunn, 1994; Xiong et al.,

Table 3
Major element compositions of experimental partial melts (wt.%).

No.	TD-06	TD-10	TD-05	TD-14	TD-13	TD-12
T (°C)	850	850	900	925	950	1000
P (GPa)	1.0	1.0	1.0	1.0	1.0	1.0
H_2O (wt.%)	2	4	2	2	0	0
t (hour)	96	96	96	120	96	96
n[a]	5	3	7	5	4	4
SiO_2	73.15(1.17)[b]	72.23(0.90)	68.23(2.33)	62.23(0.31)	57.88(0.43)	57.69(0.39)
TiO_2	0.25(0.05)	0.27(0.06)	0.46(0.15)	0.79(0.03)	1.18(0.18)	1.47(0.19)
Al_2O_3	14.73(0.64)	15.41(0.17)	15.26(0.76)	17.14(0.24)	17.76(0.19)	16.59(0.13)
FeO[c]	2.37(0.35)	2.10(0.56)	4.40(1.32)	6.80(0.17)	8.74(0.31)	6.82(0.07)
MnO	0.08(0.07)	0.07(0.13)	0.10(0.13)	0.27(0.06)	0.19(0.11)	0.11(0.09)
MgO	0.28(0.19)	0.14(0.06)	0.52(0.56)	1.49(0.07)	2.27(0.01)	4.16(0.25)
CaO	1.84(0.27)	1.88(0.17)	2.32(0.57)	4.42(0.12)	5.06(0.09)	6.74(0.11)
Na_2O	5.02(0.40)	5.42(0.39)	5.61(0.50)	5.68(0.34)	5.76(0.31)	5.26(0.15)
K_2O	2.16(0.16)	2.34(0.19)	2.95(0.36)	1.10(0.09)	1.03(0.08)	0.79(0.06)
P_2O_5	0.13(0.13)	0.14(0.12)	0.15(0.25)	0.09(0.04)	0.07(0.14)	0.26(0.19)
Total[d]	93.26	91.13	92.58	92.70	93.34	93.82
A/CNK	1.06	1.04	0.92	0.92	0.90	0.76
A/NK	1.39	1.35	1.23	1.63	1.68	1.74

No.	TD-03	TD-07	TD-24	TD-25	TD-22	TD-23
T (°C)	1000	1000	900	900	925	925
P (GPa)	1.0	1.0	1.5	1.5	1.5	1.5
H_2O (wt.%)	2	4	2	4	2	4
t (hour)	96	96	120	120	120	120
n	4	5	6	8	5	6
SiO_2	55.11(0.41)	56.07(0.44)	66.58(0.60)	66.10(0.58)	63.72(0.62)	63.68(0.54)
TiO_2	1.40(0.13)	1.37(0.07)	0.61(0.03)	0.62(0.10)	1.02(0.13)	1.02(0.08)
Al_2O_3	16.07(0.15)	16.18(0.28)	17.17(0.31)	17.35(0.45)	17.60(0.33)	17.38(0.21)
FeO	10.84(0.18)	9.35(0.21)	3.50(0.30)	3.59(0.25)	4.67(0.22)	4.73(0.08)
MnO	0.25(0.12)	0.26(0.07)	0.04(0.05)	0.09(0.10)	0.03(0.03)	0.05(0.06)
MgO	3.75(0.11)	4.16(0.28)	0.62(0.11)	0.67(0.08)	1.10(0.09)	0.99(0.07)
CaO	6.43(0.19)	6.52(0.24)	2.39(0.18)	2.55(0.12)	2.81(0.17)	2.87(0.17)
Na_2O	5.39(0.22)	4.86(0.35)	7.53(0.21)	7.49(0.39)	7.71(0.26)	7.77(0.32)
K_2O	0.64(0.09)	0.91(0.04)	1.41(0.12)	1.34(0.09)	1.22(0.08)	1.30(0.09)
P_2O_5	0.13(0.09)	0.30(0.19)	0.14(0.09)	0.21(0.14)	0.12(0.11)	0.21(0.18)
Total	93.37	94.38	93.29	91.93	93.72	94.23
A/CNK	0.76	0.78	0.94	0.94	0.92	0.90
A/NK	1.68	1.80	1.23	1.26	1.26	1.22

No.	TD-19	TD-20	TD-21	TD-16	TD-17	TD-18
T (°C)	950	950	950	975	975	975
P (GPa)	1.5	1.5	1.5	1.5	1.5	1.5
H_2O (wt.%)	0	2	4	0	2	4
t (hour)	96	96	96	96	96	96
n	7	5	7	4	5	6
SiO_2	61.26(0.50)	61.17(0.40)	62.11(0.76)	60.32(0.43)	59.42(0.19)	59.70(0.50)
TiO_2	1.40(0.08)	1.37(0.06)	1.22(0.13)	1.45(0.16)	1.54(0.09)	1.58(0.19)
Al_2O_3	17.66(0.25)	17.76(0.28)	17.03(0.36)	17.51(0.15)	17.46(0.33)	17.61(0.26)
FeO	5.62(0.48)	5.98(0.34)	5.79(0.33)	6.22(0.39)	6.54(0.27)	6.35(0.41)
MnO	0.14(0.10)	0.14(0.08)	0.09(0.06)	0.11(0.08)	0.20(0.11)	0.14(0.07)
MgO	1.70(0.20)	1.50(0.17)	1.43(0.11)	2.10(0.09)	2.24(0.17)	2.36(0.20)
CaO	3.99(0.28)	3.81(0.20)	3.62(0.13)	4.60(0.16)	5.06(0.24)	4.80(0.23)
Na_2O	7.02(0.37)	6.89(0.32)	7.10(0.33)	6.50(0.38)	6.32(0.24)	6.35(0.17)
K_2O	1.04(0.11)	1.16(0.09)	1.31(0.11)	1.01(0.06)	0.98(0.10)	0.92(0.05)
P_2O_5	0.17(0.13)	0.22(0.22)	0.29(0.21)	0.20(0.10)	0.24(0.14)	0.22(0.13)
Total	91.79	92.26	93.67	94.27	92.90	93.22
A/CNK	0.89	0.91	0.87	0.87	0.85	0.87
A/NK	1.39	1.41	1.30	1.49	1.52	1.54

No.	XD-09	XD-07	XD-04	XD-06	XD-01	XD-02	XD-03
T (°C)	900	925	950	950	975	975	975
P (GPa)	1.5	1.5	1.5	1.5	1.5	1.5	1.5
H_2O (wt.%)	4	4	0	4	0	2	4
t (hour)	120	120	96	96	96	96	96
n	8	6	4	3	4	5	4
SiO_2	64.46(0.37)	62.06(0.54)	57.90(0.78)	56.76(0.52)	56.11(0.47)	55.53(0.71)	56.05(0.07)
TiO_2	0.74(0.10)	1.00(0.10)	1.20(0.06)	1.47(0.13)	1.16(0.08)	1.26(0.12)	1.22(0.05)
Al_2O_3	19.57(0.34)	19.45(0.46)	21.01(0.10)	21.14(0.57)	20.54(0.13)	20.09(0.66)	20.38(0.31)
FeO	2.23(0.24)	2.74(0.24)	3.26(0.24)	4.18(0.16)	4.22(0.41)	4.80(0.30)	4.71(0.30)
MnO	0.09(0.09)	0.02(0.03)	0.02(0.02)	0.14(0.03)	0.14(0.04)	0.17(0.08)	0.17(0.10)

(*continued on next page*)

Table 3 (*continued*)

No.	XD-09	XD-07	XD-04	XD-06	XD-01	XD-02	XD-03
T (°C)	900	925	950	950	975	975	975
P (GPa)	1.5	1.5	1.5	1.5	1.5	1.5	1.5
H_2O (wt.%)	4	4	0	4	0	2	4
t (hour)	120	120	96	96	96	96	96
n	8	6	4	3	4	5	4
MgO	1.22(0.12)	1.82(0.19)	3.43(0.53)	3.72(0.12)	4.38(0.19)	4.29(0.20)	4.17(0.22)
CaO	5.30(0.21)	6.75(0.20)	9.16(0.60)	7.58(0.50)	9.27(0.36)	9.55(0.34)	9.13(0.24)
Na_2O	4.75(0.24)	4.08(0.34)	2.97(0.08)	3.90(0.07)	3.11(0.25)	3.24(0.16)	3.17(0.24)
K_2O	1.51(0.09)	1.81(0.07)	0.85(0.20)	0.81(0.16)	0.87(0.13)	0.89(0.04)	0.79(0.07)
P_2O_5	0.13(0.11)	0.23(0.20)	0.13(0.12)	0.16(0.27)	0.21(0.18)	0.17(0.12)	0.23(0.06)
Total	89.37	90.09	87.51	88.53	88.84	88.02	90.49
A/CNK	1.03	0.93	0.94	1.00	0.90	0.85	0.90
A/NK	2.07	2.24	3.62	2.90	3.39	3.19	3.36

Note: a, the number of analytical points; in each experimental product; b, the average value of the electronic probe analysis data after normalization, the values in theparenthesis refer to the standard deviation; c, all Fe as FeO; d, total gives original total.

2005), melting is sufficient to approach equilibrium where T ≥ 900 °C and the run time is ≥96 h. In the present study, only two runs were conducted at 850 °C, with most runs conducted at sufficiently high temperatures (T ≥ 900 °C) to result in equilibrium being attained within 96 h. Equilibrium was also confirmed by comparing the compositions of minerals and melts at different locations in the experimental products. The major and trace element compositions at different sites are homogeneous (within analytical error), indicating that equilibrium was attained. Furthermore, the garnet–pyroxene Fe^{2+}–Mg geothermometer was used to examine whether equilibrium was attained (Table 5). It is clear that the temperatures for the selected runs and those estimated by the geothermometer (Ravna, 2000) are similar, suggesting that the experiments attained, or were close to, equilibrium. Fe–Mg exchange distribution coefficients ($K_{d,\ Fe–Mg}$) of mineral–melt (Amp, Cpx, and Grt) were also calculated (***S1-Table 6***). The $K_{d,\ Fe–Mg}$ values are acceptable, apart from the runs at 850 °C, demonstrating that most runs were close to equilibrium.

4.2. *Effects of small amounts of sediment addition during partial melting of basaltic rocks*

To assess the effects of the addition of a small amount of sediment during the partial melting of basaltic rock (basalt/amphibolite), several studies of the partial melting of basalts at 0.6–2.0 GPa and 800–1125 °C were chosen for comparison (Beard and Lofgren, 1991; Blatter et al., 2013, 2017; Nandedkar et al., 2014; Qian and Hermann, 2013; Rapp and Watson, 1995; Rapp et al., 1991; Sen and Dunn, 1994; Sisson et al., 2005; Xiong et al., 2005, 2006). Compared with our experiments, the runs chosen from the other studies had similar experimental *P–T* conditions and starting materials (basalts or metabasalts), apart from the sediment addition in our runs. The results of the previous studies can be regarded as baseline compositions against which to assess the effects of sediment addition.

4.2.1. *Chemical compositions of the starting materials*

Sediment addition makes the starting mixture enriched in SiO_2 and $Na_2O + K_2O$ as compared with the basalt and amphibolite (Table 1; Fig. 2). The mudstone JS41 has a relatively high LOI value (up to 5.7 wt %), which mainly reflects the presence of H_2O (or OH^-), and therefore sediment addition makes the starting mixture hydrous (~0.5 wt% water content) even without water addition. Sediment addition also changed the trace element composition of the starting mixture. JS41 is enriched in Rb, Th, U, La, and Ce, and this results in the starting mixtures being enriched in these elements as compared with the basalt and amphibolite (KL24 and QS08-1; Table1).

4.2.2. *Residual minerals*

The experimental products of this study have phase assemblages similar to those of previous studies, mainly Melt ± Amp ± Pl ± Cpx ± Grt (Fig. 5). However, the stabilities of these four major minerals are very different from those reported in previous studies. Amp and Pl are present in the starting amphibolite (QS08-1), whereas Cpx and Pl are present in the starting basalt (KL24). Amp disappeared in the partial melting runs of mixture QS at > 925–950 °C and 1.0–1.5 GPa, whereas it was stabilized at > 1000 °C in partial melting runs of amphibolite at similar pressures. Pl disappeared in partial melting runs of mixture QS at > 950 °C and 1.0 GPa, and this temperature is much lower than for plagioclase exhaustion at ~1200 °C during partial melting of hydrous amphibolite and ~1050 °C during dehydration melting experiments of amphibolite. Pl was completely exhausted in runs of mixtures QS and KL at 1.5 GPa, similar to dehydration melting experiments on amphibolite, but this temperature is much lower than for partial melting of hydrous amphibolite (Fig. 5). Cpx was a new crystalline phase for runs on mixture QS, but a residual phase for runs on mixture KL. However, Cpx proportions in runs on mixture QS have almost the same range as in runs on mixture KL. The Cpx-in temperature from our study is much lower than that in previous studies at 1.0 GPa, whereas our Cpx-in temperature is intermediate between the results from partial melting of hydrous amphibolite and dehydration melting experiments on amphibolite at 1.5 GPa (Fig. 5). Grt is also a new crystalline phase in our experiments, and its lowest crystallization temperature is higher than that of the partial melting of amphibolite (Fig. 5).

4.2.3. *Melting percentage*

The addition of sediment to amphibolite also produced more melt during partial melting experiments at temperatures of > 900 °C (Fig. 6). The melt percentage is also influenced by the run pressure, mineral assemblage, and major element composition. Runs on the mixture QS at 1.0 GPa have a higher melt percentage than at 1.5 GPa at ~925 °C (Fig. 6). The mineral assemblage also affects the melt percentage, with runs on the mixture QS at 1.5 GPa having a higher melt percentage than those on mixture KL at 1.5 GPa. The minerals present in amphibolite QS08-1 are mainly Amp and Pl, whereas basalt KL24 contains mainly Cpx and Pl. Although the basalt contains some glass, the fusible Amp (as compared with Cpx) means the amphibolites produces more melt than the basalt at 1.5 GPa. Some fusible elements (e.g., Na and K) might also contribute to the higher melt percentage, with the effects being as follows: these incompatible elements tends to enter the melt during partial melting, particularly at low degrees of partial melting, such as Na for the runs at 0.69 GPa and 850 °C reported by Beard and Lofgren (1991).

We now compare our results with those obtained by melting pure basalt/amphibolite. The proportion of melt produced by the partial melting of anhydrous basalt increases smoothly with temperature (Sen and Dunn, 1994; Sisson et al., 2005), whereas the partial melting of

Table 4
Trace-elements compositions of experimental partial melts (ppm).

No.	TD-14	TD-13	TD-07	TD-24	TD-25	TD-22	TD-23	TD-19
T (°C)	925	950	1000	900	900	925	925	950
P (GPa)	1.0	1.0	1.0	1.5	1.5	1.5	1.5	1.5
H_2O (wt.%)	2	0	4	2	4	2	4	0
t (hour)	120	96	96	120	120	120	120	96
n	5	5	5	5	5	4	4	5
Sc	44.1	23.3	34.1	32.5	36.7	32.0	43.7	31.2
V	469	100	328	309	320	237	352	307
Cr	17.1	2.31	11.3	9.92	12.6	9.87	13.1	14.3
Co	36.0	18.8	23.7	29.9	27.1	24.4	35.4	25.7
Ni	14.9	2.05	1.91	4.45	7.30	6.51	8.41	9.38
Cu	0.798	0.255	0.301	0.407	0.730	1.33	1.19	0.449
Zn	134	128	113	114	121	114	107	103
Ga	22.3	22.3	20.0	24.6	23.5	23.5	23.3	23.4
Rb	25.0	36.9	36.3	33.1	28.3	29.8	26.4	25.8
Sr	465.	637	483	611	627	640	494	617
Y	29.6	29.0	25.7	28.4	27.3	28.0	38.7	21.2
Zr	88.0	96.9	78.7	99.6	94.3	92.4	87.0	85.5
Nb	2.36	2.90	2.33	2.32	2.81	2.55	2.58	2.54
Sn	0.970	1.96	1.57	1.58	1.04	1.12	1.75	1.01
Cs	2.25	3.79	3.91	3.62	2.99	3.17	2.74	2.80
Ba	217	275	197	285	261	268	211	252
La	14.0	25.1	11.2	16.5	16.9	14.9	12.2	16.6
Ce	33.5	54.8	26.1	35.3	37.9	33.2	28.7	37.5
Pr	4.20	6.33	3.18	4.24	4.65	3.95	3.34	4.60
Nd	18.3	25.6	14.6	18.1	19.5	17.3	15.5	19.4
Sm	5.38	5.62	3.52	4.61	5.24	4.53	4.55	5.03
Eu	1.32	1.72	1.18	1.44	1.59	1.46	1.48	1.30
Gd	6.04	5.64	4.47	4.70	5.85	5.16	6.15	5.14
Tb	0.945	0.913	0.675	0.708	0.791	0.775	0.984	0.714
Dy	5.48	5.70	4.47	4.76	5.16	5.14	6.79	3.78
Ho	1.12	1.14	0.95	1.19	1.01	1.01	1.31	0.80
Er	3.33	2.92	2.70	3.18	3.10	2.73	4.22	2.16
Tm	0.410	0.394	0.390	0.492	0.402	0.376	0.602	0.316
Yb	3.10	2.79	2.61	2.93	2.81	3.12	4.06	2.22
Lu	0.422	0.464	0.438	0.474	0.446	0.427	0.603	0.321
Hf	2.78	2.97	2.05	2.41	2.78	2.40	2.41	2.65
Ta	0.135	0.181	0.173	0.188	0.157	0.165	0.192	0.162
Pb	5.51	14.6	14.9	7.86	7.77	7.44	8.05	7.58
Th	1.42	2.40	1.38	1.70	1.63	1.50	1.13	1.51
U	0.537	0.838	0.476	0.760	0.681	0.597	0.648	0.644

No.	TD-21	TD-16	TD-17	TD-18
T (°C)	950	975	975	975
P (GPa)	1.5	1.5	1.5	1.5
H_2O (wt.%)	4	0	2	4
t (hour)	96	96	96	96
n	4	4	4	4
Sc	50.3	47.8	34.2	45.9
V	437	478	331	444
Cr	15.3	20.7	12.8	18.5
Co	37.7	29.2	22.0	27.4
Ni	9.56	6.60	5.85	7.33
Cu	1.19	1.39		0.506
Zn	113	104	105	102
Ga	21.2	23.6	21.9	21.6
Rb	24.2	21.6	23.4	24.1
Sr	433	528	539	527
Y	43.7	43.2	26.8	36.8
Zr	81.3	85.9	80.9	83.9
Nb	1.78	2.11	2.17	2.40
Sn	1.57	0.918	1.10	1.18
Cs	2.55	2.38	2.49	2.40
Ba	178	209	213	207
La	10.4	15.4	15.0	14.8
Ce	24.1	35.7	33.8	33.3
Pr	2.95	4.27	4.06	4.10
Nd	15.4	18.4	18.2	17.3
Sm	4.57	4.64	4.22	4.45
Eu	1.49	1.44	1.31	1.43
Gd	6.40	6.09	5.56	5.90
Tb	1.10	1.07	0.699	0.928
Dy	7.57	7.47	5.18	6.37
Ho	1.67	1.70	1.02	1.47

Table 4 (*continued*)

No.	TD-21	TD-16	TD-17	TD-18
T (°C)	950	975	975	975
P (GPa)	1.5	1.5	1.5	1.5
H_2O (wt.%)	4	0	2	4
t (hour)	96	96	96	96
n	4	4	4	4
Er	4.66	4.48	2.78	3.96
Tm	0.752	0.700	0.424	0.604
Yb	5.20	5.41	2.94	4.58
Lu	0.672	0.778	0.411	0.705
Hf	2.14	2.69	2.53	2.56
Ta	0.129	0.152	0.177	0.139
Pb	7.48	7.53	7.24	6.86
Th	1.16	1.33	1.38	1.53
U	0.446	0.609	0.563	0.680

hydrous basalt (Qian and Hermann, 2013; Xiong et al., 2005) and hydrous basaltic glass (Blatter et al., 2013, 2017; Nandedkar et al., 2014) is characterized by abrupt increases in melt proportion. Partial melting of our mixtures exhibits a similar abrupt melt increase as for the hydrous basalt, but at lower temperatures (900–925 °C). Crystallization experiments on hydrous basaltic glass have shown that the melt proportion has an inverse correlation with the Pl + Amp content (Blatter et al., 2013, 2017; Nandedkar et al., 2014). The addition of sediment results in the residual minerals (Amp + Pl) being less stable at > 900 °C and having relatively lower liquidus temperatures in the mixtures (Fig. 5). The addition of sediments also makes the mixtures enriched in fusible elements (e.g., Na and K; Table 1), thereby increasing the melting percentage. Our results are similar to those of Mccarthy and Patiño Douce (1997), in that the melt percentage is enhanced at the contact between basalt and sediment.

4.2.4. Major element compositions of the partial melts

Sediment addition not only affects the phase assemblages of the experimental products, but also the chemical compositions of the minerals and partial melts. To account for the effect of the differences in starting materials, we used the melt/starting material elemental ratio (MSR). The MSR values of amphibolite and our mixtures are similar for FeO and CaO (Fig. 9D and F), which indicates that sediment addition has little effect on these elements. The MSR for SiO_2 in the partial melts of the mixtures is lower than the values for amphibolite at a given temperature, when the run temperature is 900–1000 °C. This indicates that even a small amount of sediment addition (10 wt%) will significantly reduce the SiO_2 content in the partial melts (Fig. 9A) at 900–975 °C and 1.0–1.5 GPa. The MSR values for Al_2O_3 in the partial melts of the mixtures are higher than those from pure amphibolite at 900–975 °C and 1.0–1.5 GPa (Fig. 9C). The low MSR for SiO_2 and high MSR for Al_2O_3 in the partial melts of the mixtures are most likely caused by the high degree of partial melting in this *P–T* range. As discussed above, sediment addition lowered the liquidus temperatures of Amp, Cpx, and Pl. Amp and Cpx are depleted in SiO_2 and Pl is enriched in Al_2O_3. The MSR values of MgO in the partial melts of the mixtures are higher at 1000 °C than for partial melting of pure amphibolite, which is again caused by the high degree of partial melting (Fig. 9E). The MSR for K_2O in the partial melts of the mixtures has a higher value than for partial melting of pure amphibolite at < 900 °C, owing mainly to sediment partial melting.

4.2.5. Trace element compositions of the partial melts

Sediment addition also affects the trace element compositions of the partial melts. Partial melts of amphibolites have similar trace element patterns as the starting material, apart from the heavy REE (Fig. 8), which are affected by residual garnet and rutile (Qian and Hermann, 2013; Rapp and Watson, 1995; Rapp et al., 1991; Xiong et al., 2005, 2006), whereas the partial melts of mixture QS are enriched in Rb, Th,

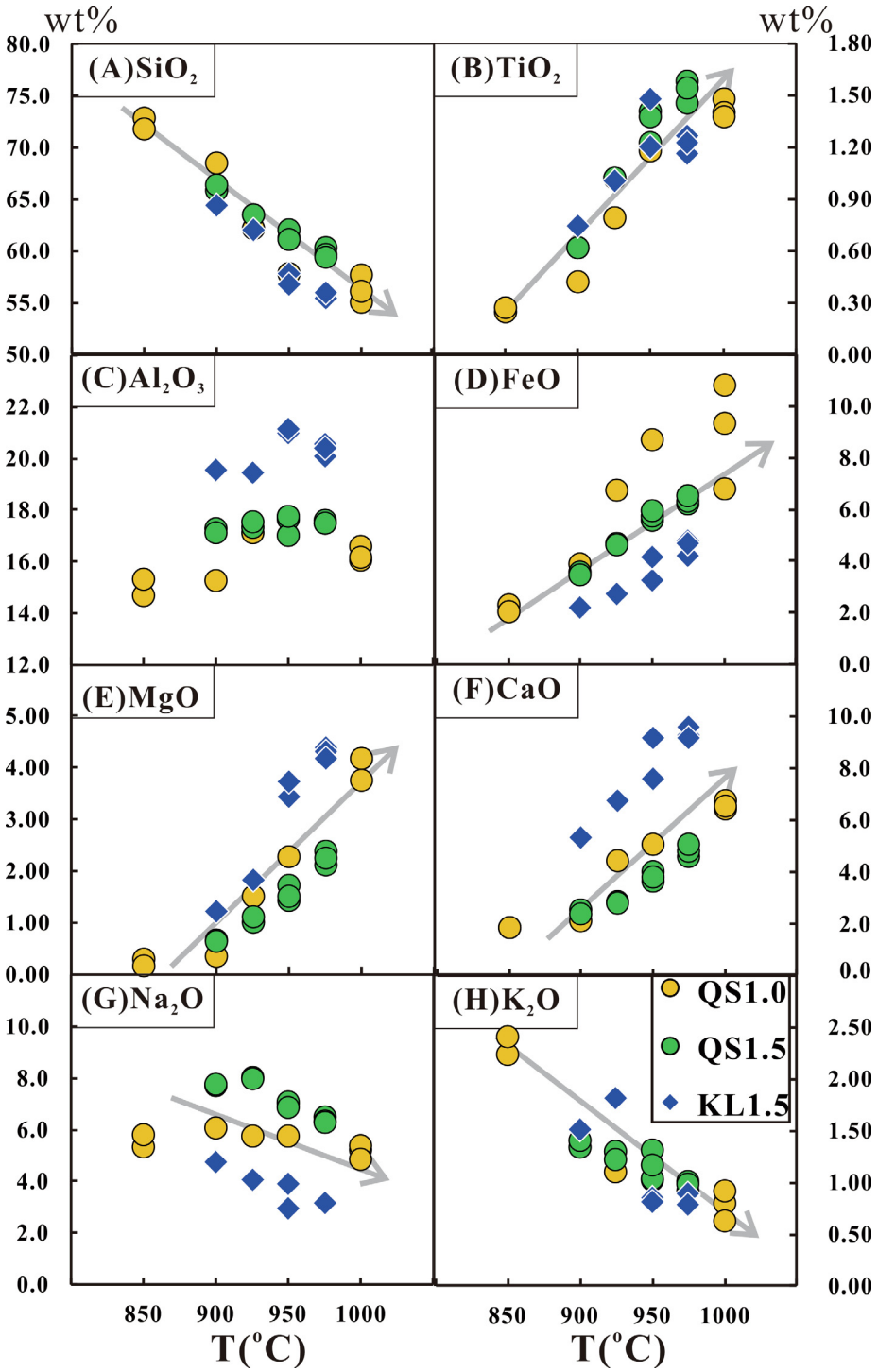

Fig. 7. Plots of oxide abundance of partial melts from mixture. QS 1.0, partial melts on mixture QS at 1.0 GPa in this study; QS 1.5, partial melts on mixture QS at 1.5G Pa in this study; KL 1.5, partial melts on mixture KL at 1.5 GPa in this study. The arrows mark the variation trend of oxide abundance in partial melts reported in this study as temperature rising.

U, and light REE (La–Eu) as compared with the starting amphibolite. These elements (Rb, Th, U, and light REE) are enriched in terrigenous sediments (Johnson and Plank, 2000; Hermann and Spandler, 2008 and references therein) and so their contents in partial melts of the amphibolite–sediment mixture are higher than those in partial melts from pure amphibolites (Fig. 8A). The sediment is enriched in light REE, with concentrations several times higher than in the amphibolite (Table 1); consequently, 10% sediment addition results in a marked change in the REE abundances in the mixture. The partial melts of the mixtures are enriched in light REE and differ from the flat REE patterns of the starting amphibolite and mixture QS (Fig. 8B).

4.3. Geological implications

The addition of sediment has a significant effect on partial melts of basaltic rocks, particularly in terms of major and trace element compositions. The role of sediment addition during the generation of granites in east Junggar, Xinjiang, northwest China is discussed in this

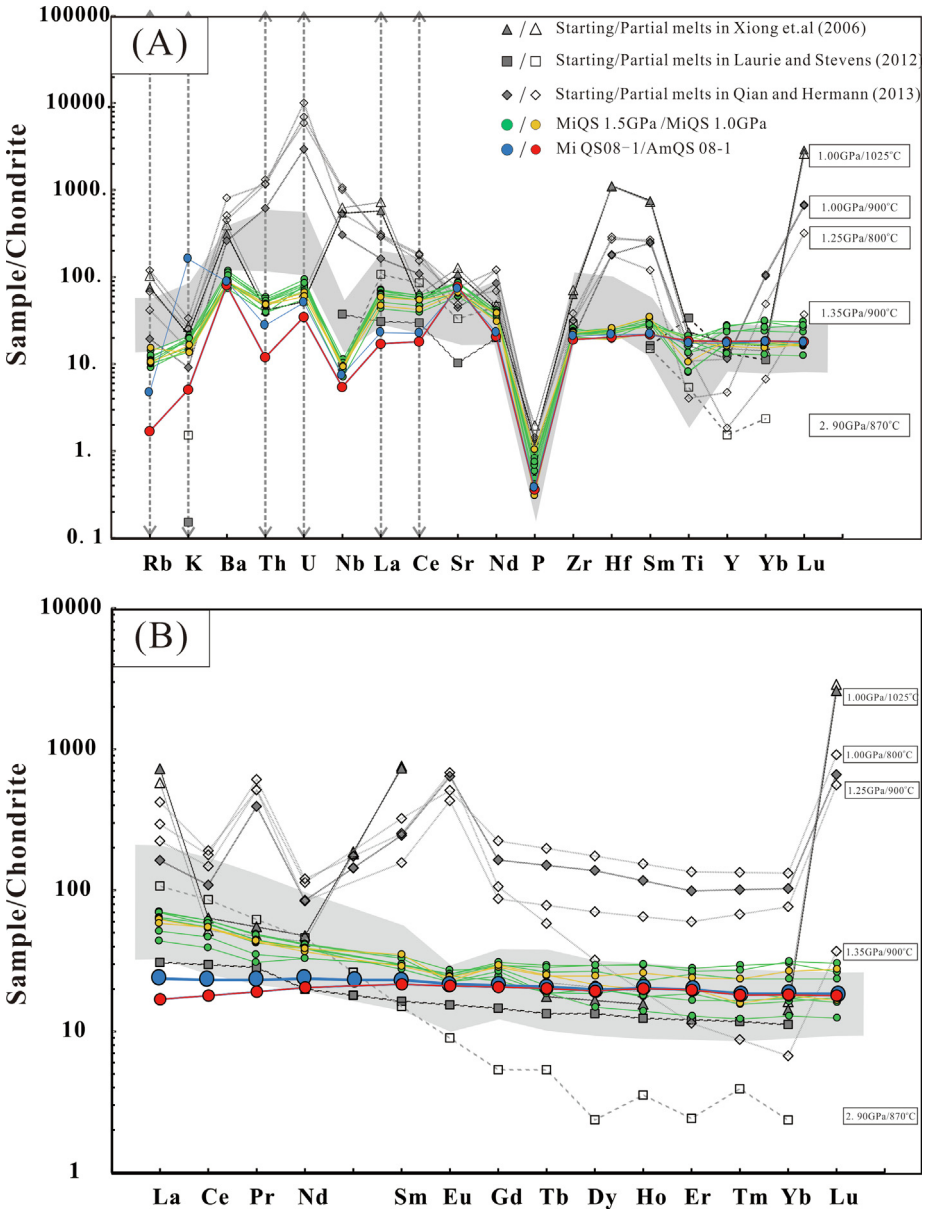

Fig. 8. Chondrite normalized spidergrams (A) and REE patterns (B) of the partial melts and field observed rocks. C1-Chondrite data are follow Sun and Mcdonough (1989). Field observation data of calc-alkaline granitic intrusives located in east Junggar (Chen and Jahn, 2004; Su, 2007; Yang et al., 2011) is shown via light grey shadow. Representative runs from partial melting experiments on basalts at 1.0–2.9 GPa (Laurie and Stevens, 2012; Qian and Hermann, 2013; Xiong et al., 2006) are compared with this study, their run conditions are listed in the boxes beside the curves.

Table 5
Calculated temperatures in selected runs.

No.	Given T (°C)	P (GPa)	H_2O (wt.%)	Estimated T[a] (°C)
TD17	975	1.5	2	986
TD22	925	1.5	2	931

Note: The temperature calculation follows the geothermometer estimated by Ravna (2000).

section. The calc-alkaline granitic rocks were probably generated via partial melting of subducted oceanic crust, with a similar chemical composition to that of basaltic rocks in the Kalamali ophiolite (Gan et al., 2010; Han et al., 1997; Tang et al., 2008). The major element compositions of these intrusive rocks are compared with the experimental partial melts of basalt and our mixtures in total alkalis–silica (TAS), A/NK–A/CNK, and Harker diagrams (Figs. 10 and 11). The data for the granitic rocks in the TAS diagram are consistent with the partial melts of mixture QS at 1.5 GPa (Fig. 10A), as well as the range of partial melts of anhydrous basalt. In the A/NK–A/CNK diagram, the data for the granitic rocks are only consistent with the partial melts of mixture QS and are distinct from the partial melts of mixture KL and amphibolites (Fig. 10B). Partial melts of hydrous basalts are compositionally similar to those of the intrusive rocks in terms of FeO versus SiO_2 (Fig. 11B), whereas partial melts of anhydrous basalts are compositionally similar to those of the intrusive rocks in terms of MgO versus SiO_2 (Fig. 11C). In other Harker diagrams, the partial melts of basalts do not compositionally match the granitoids. However, the partial melts of mixture QS at 1.5 GP are ported in this paper are compositionally similar to those of the granitoids in all Harker diagrams. As such, these post-collisional granitic rocks might have been generated by the melting of an amphibolite–sediment mixture.

Partial melts of a mixture of amphibolite and sediment match those of the intrusive rocks in terms of trace elements (Fig. 8). Partial melts of amphibolites typically have trace element compositions similar to their

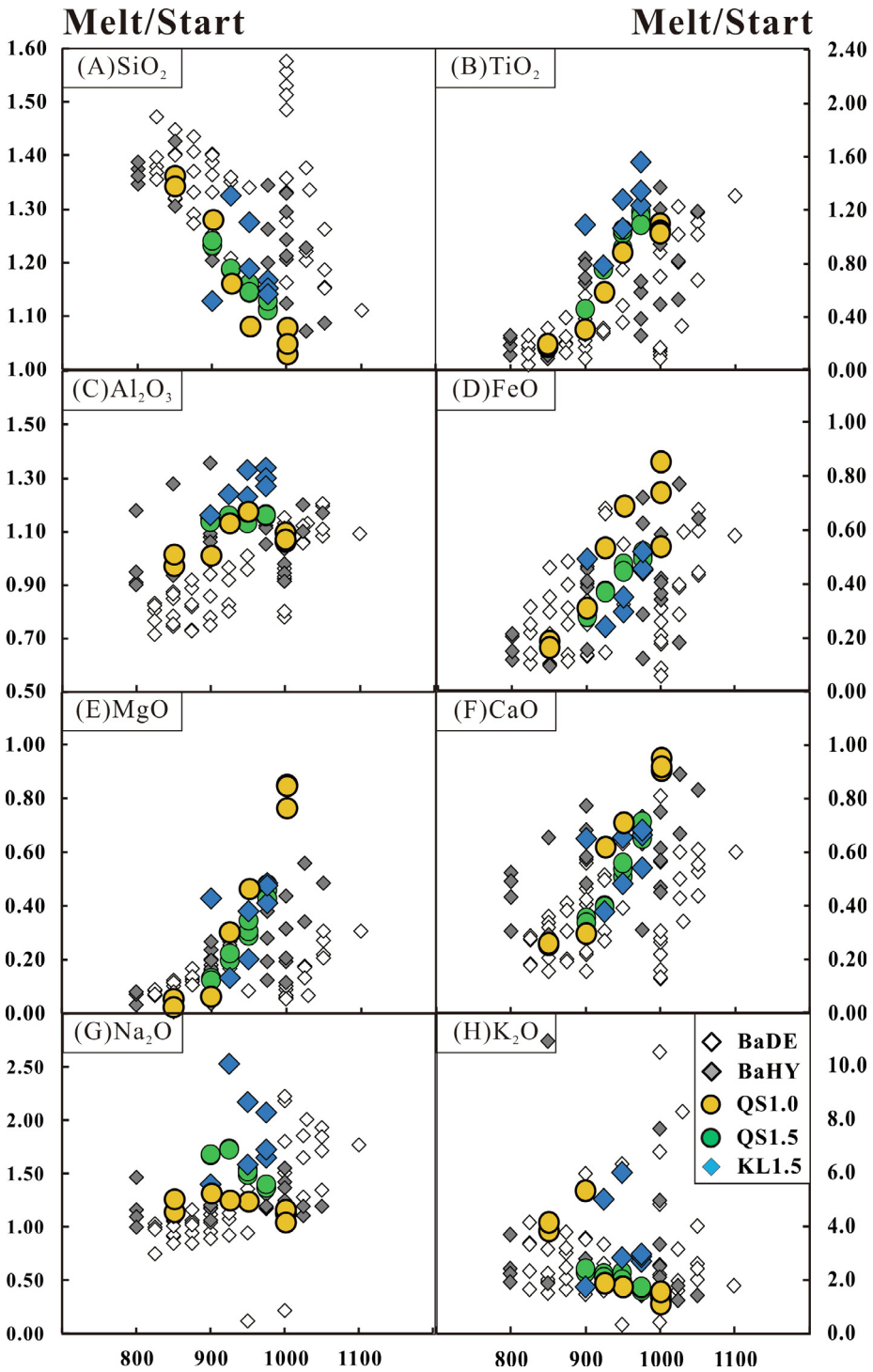

Fig. 9. Ratios of oxide abundance in partial melts and those in their starting basalts. QS 1.0, partial melts on mixture QS at 1.0 GPa in this study; QS 1.5, partial melts on mixture QS at 1.5 GPa in this study; KL 1.5, partial melts on mixture KL at 1.5 GPa in this study. BaDE, Melts generate in dehydration melting experiments on basalts; BaHY, Melts generate in partial melting of hydrous basalt (Beard and Lofgren, 1991; Qian and Hermann, 2013; Rapp and Watson, 1995; Rapp et al., 1991; Rushmer, 1991; Sisson et al., 2005; Takahahshi et al., 1998; Xiong et al., 2005, 2006; Yaxley and Green, 1998).

source, except for some elements (e.g., Eu and heavy REE), which are affected by residual minerals. The amphibolite (QS08-1) from the Kalamali ophiolite and nearby granitic rocks exhibit significant differences in Rb, Th, U, La, and Ce contents and patterns (Fig. 8A), whereas partial melts of mixture QS are compositionally similar to those of the intrusive rocks. The chondrite-normalized REE patterns of the source amphibolite are flat (Fig. 8B), whereas the patterns of the partial melts of the basalt–sediment mixture are enriched in light REE. Data for the granitic rocks are also consistent with the partial melts of mixture QS in Sr/Y–Y and La_N/Yb_N–Yb_N diagrams (Fig. 12), whereas the partial melts of amphibolite have adakitic characteristics at 800–1050 °C and 1.0–1.5 GPa, indicatingthat sediment addition obscures the adakitic features at 850–1000 °C and 1.0–1.5 GPa (i.e., at the *P–T* conditions of the lower crust). The high Y contents, low Sr/Y ratios, and very low La_N/Yb_N ratios are key features of melts where sediment has been added to the source. Notably, sediment addition enables the generation of granites

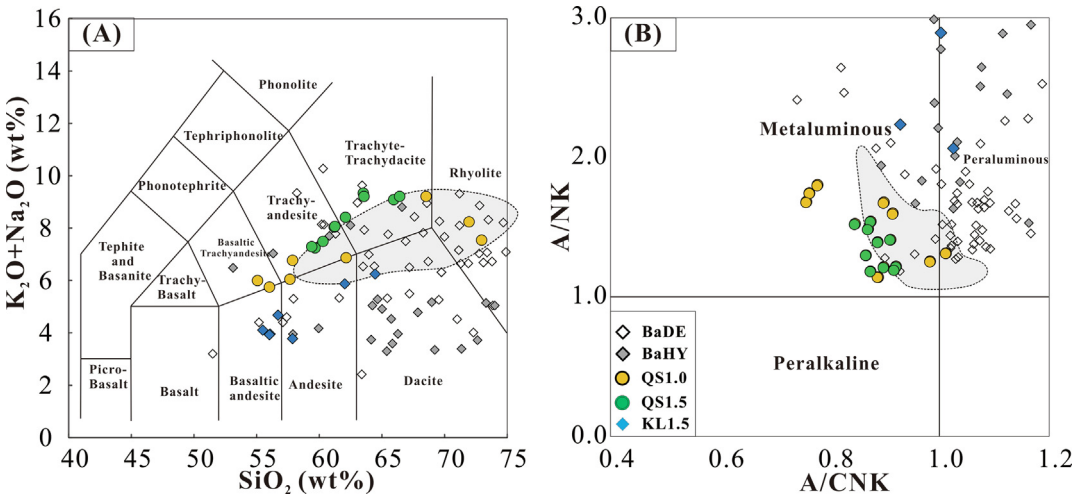

Fig. 10. Total alkali versus silica (TAS) variation diagram (A) and A/NK versus A/CNK diagram (B) of partial melts from basalts and field observation. Classification and nomenclature of TAS diagram follow Maitre (1989). Symbols of BaDE, BaHY, QS 1.0, QS 1.5 and KL 1.5 are the same as in Fig. 9; the data of BaDE and BaHY are also from the same references as Fig. 9. The variation ranges of calc-alkaline granitic intrusives located in east Junggar (Chen and Jahn, 2004; Gan et al., 2010; Gao and Ma, 2013; Han et al., 1997; Su, 2007; Yan et al., 2008; Yang et al., 2011) are shown via light grey shadow.

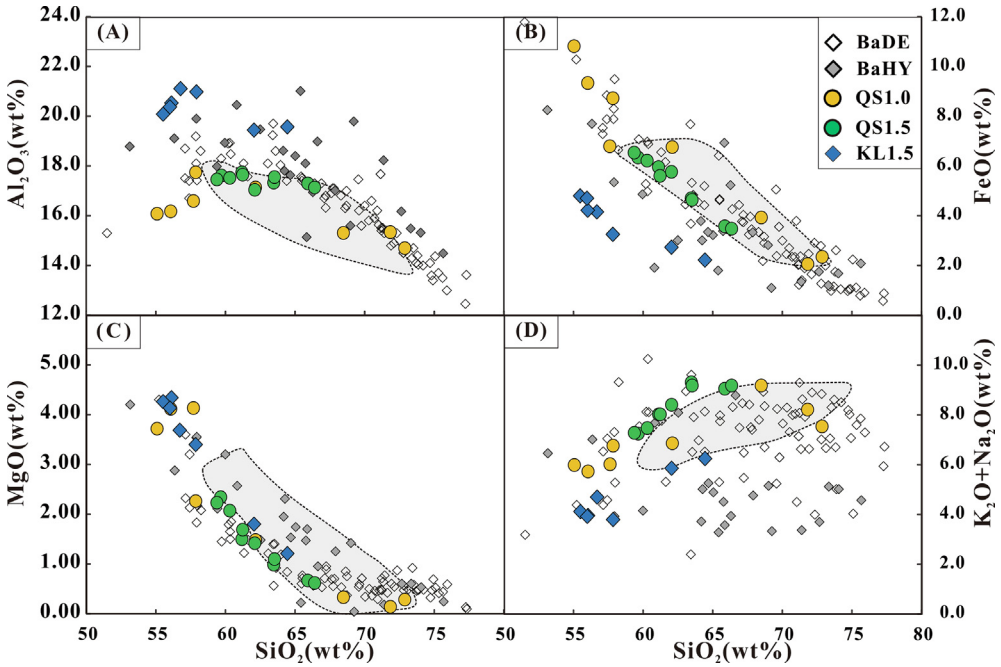

Fig. 11. Harker diagrams of partial melts from basalts and field observation. Symbols are the same as in Fig. 10; the data of partial melts from pure basalts and field observation are from the same reference as in Fig. 10.

without adakitic features and lowers the melting temperature of subducted oceanic crust, which can result in the generation of voluminous granitic magmas. This scenario is consistent with the composition of granitic intrusive rocks in east Junggar, northwest China.

5. Conclusions

Our experiments revealed that the addition of small amounts (10 wt %) of sediment has a marked effect on the partial melting of basalt in terms of the chemical composition of experimental partial melts produced from amphibolite/basalt–mudstone mixtures at 850–1000 °C and 1.0–1.5 GPa. The importance of sediment addition was also verified and identified in a case study from east Junggar, Xinjiang, China. The main conclusions of this study are follows.

1. Sediment addition changes the stability fields of four major phases (Amp + Pl + Grt + Cpx), resulting in the residual minerals (Amp + Pl) having lower liquidus temperatures and inhibiting the crystallization of new phases (Grt + Cpx). This produces a higher degree (> 50%) of melting for basalt/amphibolite–mudstone mixtures at 900–975 °C and 1.0–1.5 GPa than for basalt/amphibolite.
2. The partial melts of the mixtures are depleted in SiO_2 and enriched in Al_2O_3 as compared with partial melts of basalt at the same P–T conditions of 900–975 °C and 1.0–1.5 GPa. Partial melts of the mixtures are enriched in Rb, Th, U, and light REE due to sediment addition.
3. Granitic magma generation by the partial melting of oceanic crust affected by sediment addition is difficult to identify using a single geochemical indicator. Sediment addition can be detected using TAS, A/NK–A/CNK, and Harker diagrams. Sediment addition results

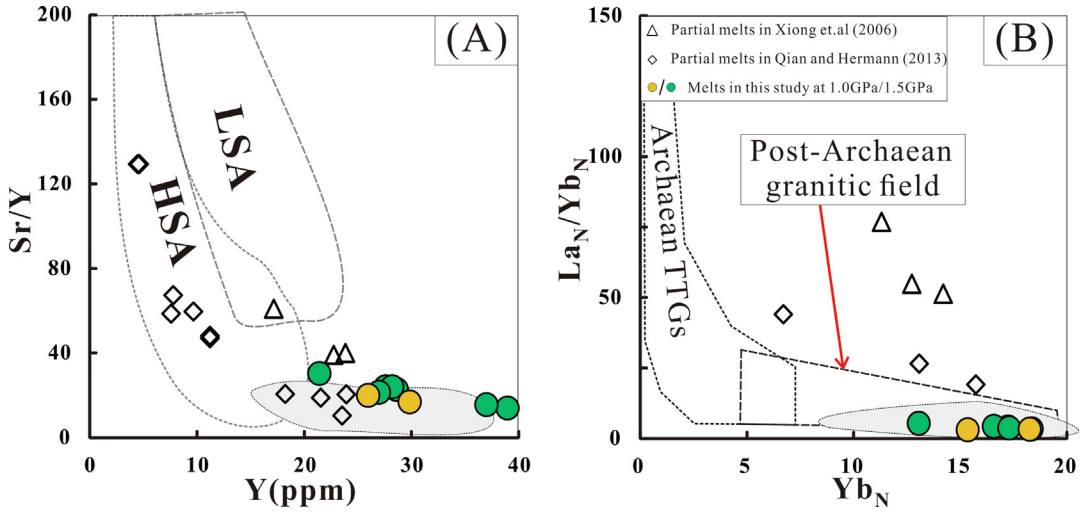

Fig. 12. Plots of Sr/Y vs. Y (A) (after Martin et al. (2005)) and La_N/Yb_N vs. Yb_N (B) (after Martin (1986). Symbols are the same as in Fig. 10, the field observation data of calc-alkaline granitoids located in east Junggar (Chen and Jahn, 2004; Su, 2007; Yang et al., 2011) is shown by light grey shadow. Partial melts from experiments on basalts (Qian and Hermann, 2013; Xiong et al., 2006) are compared with this study. LSA: Low-SiO_2 adakites; HAS: high-SiO_2 adakites.

in partial melts that are enriched in Rb, Th, U, and light REE, and characterized by high Y contents, low Sr/Y and very low La_N/Yb_N ratios.

Declaration of Competing Interest

The authors declare that they have no known competing financial interests or personal relationships that could have appeared to influence the work reported in this paper.

Acknowledgements

We thank Gerhard Brey for his guidance in improving this paper, and Wenge Zhou and Qiao Shu for useful discussions. Constructive comments from Thomas Sisson also helped to improve the paper. This work was financially supported by the Natural Science Foundation of China (41502057 and 41172071) and the Foundation of Suzhou University (KJ2017A444, 2015jb01, 2015jb07, and 2019ZD46).

Appendix A. Supplementary material

Supplementary data to this article can be found online at https://doi.org/10.1016/j.jseaes.2019.104111.

References

Allègre, C.J., 1988. The behavior of the earth: continental and seafloor mobility. J. Membr. Biol. 146, 239–251.
Anderson, D.L., 2007. New Theory of the Earth. Cambridge University Press.
Beard, J.S., Lofgren, G.E., 1991. Dehydration melting and water-saturated melting of basaltic and andesitic greenstones and amphibolites at 1, 3, and 6. 9 kb. J. Petrol. 32, 465–501.
Blatter, Dawnika, L., Sisson, Thomas, W., Hankins, B., 2013. Crystallization of oxidized, moderately hydrous arc basalt at mid- to; lower-crustal pressures: implications for andesite genesis. Contribut. Mineral. Petrol. 166, 861–886.
Blatter, D.L., Sisson, T.W., Hankins, W.B., 2017. Voluminous arc dacites as amphibole reaction-boundary liquids. Contrib. Miner. Petrol. 172, 27.
Chen, B., Jahn, B.M., 2004. Genesis of post-collisional granitoids and basement nature of the Junggar Terrane, NW China: Nd–Sr isotope and trace element evidence. J. Asian Earth Sci. 23, 691–703.
Coleman, R.G., 2012. Ophiolites: Ancient Oceanic Lithosphere? Springer Science & Business Media.
Dai, L.Q., Zheng, F., Zhao, Z.F., Zheng, Y.F., 2017. Recycling of Paleotethyan oceanic crust: geochemical record from postcollisional mafic igneous rocks in the Tongbai-Hong'an orogens. Geol. Soc. Am. Bull. 129 (B31461), 31461.
Dilek, Y., Furnes, H., 2014. Ophiolites and their origins. Elements 10, 93–100.
Dilek, Y., Newcomb, S., 2003. Ophiolite concept and the evolution of geological thought.
Frisch, W., Meschede, M., Blakey, R., 2011. Plate tectonics: Continental drift and mountain building.
Fu, H., Zhu, C., 1986. Ultra-high pressure measurement technology and experimental study on mantle minerals (in Chinese). Earth Environ. 47–50.
Gan, L., Tang, H., Han, Y., 2010. Geochronology and geochemical characteristics of Yemaquan granitic pluton in East Junggar, Xinjiang. Acta Petrol. Sin. 26, 2374–2388.
Gao, S.L., Ma, Q.-Y., 2013. LA-ICP MS dating of zircon from the Aotawuke'erxi granite mass in Kalamaili area and its geochemical characteristic. Xinjiang Geol. 31, 1–5.
Han, B., Ji, J., Song, B., Chen, L., Zhang, L., 2006. Late Paleozoic vertical growth of continental crust around the Junggar Basin, Xinjiang, China (Part I): timing of post-collisional plutonism. Acta Petrol. Sin. 22, 1077–1086.
Han, B.F., Wang, S.G., Jahn, B.M., Hong, D.W., Kagami, H., Sun, Y.L., 1997. Depleted-mantle source for the Ulungur River A-type granites from North Xinjiang, China: geochemistry and Nd–Sr isotopic evidence, and implications for Phanerozoic crustal growth. Chem. Geol. 138, 135–159.
Hermann, J., Spandler, C.J., 2008. Sediment melts at sub-arc depths: an experimental study. J. Petrol. 49, 717–740.
Hu, Y., Teng, F.Z., Plank, T.A., Huang, K.J., 2017. Magnesium isotopic composition of subducting marine sediments. Chem. Geol.
Huang, X.L., Xu, Y.G., Lo, C.H., Wang, R.C., Lin, C.Y., 2007. Exsolution lamellae in a clinopyroxene megacryst aggregate from Cenozoic basalt, Leizhou Peninsula, South China: petrography and chemical evolution. Contrib. Miner. Petrol. 154, 691–705.
Huene, R., Scholl, D.W., 1991. Observations at convergent margins concerning sediment subduction, subduction erosion, and the growth of continental crust. Rev Geophys. Rev. Geophys. 29, 279–316.
Johnson, M.C., Plank, T., 2000. Dehydration and melting experiments constrain the fate of subducted sediments. Geochem. Geophys. Geosyst. 1, 597.
Koepke, J., Feig, S.T., Snow, J., Freise, M., 2004. Petrogenesis of oceanic plagiogranites by partial melting of gabbros: an experimental study. Contrib. Miner. Petrol. 146, 414–432.
Laurie, A., Stevens, G., 2012. Water-present eclogite melting to produce Earth's early felsic crust. Chem. Geol. 314–317, 83–95.
Liu, X.J., Xu, J., Hou, Q., Bai, Z., Lei, M., 2007. Geochemical characteristics of Karamaili ophiolite in east Junggar, Xingjiang: products of ridge subduction (in Chinese with English abstract). Acta Petrol. Sin. 23, 1591-1602.
Liu, Y., Hu, Z., Gao, S., Günther, D., Xu, J., Gao, C., Chen, H., 2008. In situ analysis of major and trace elements of anhydrous minerals by LA-ICP-MS without applying an internal standard. Chem. Geol. 257, 34–43.
Maitre, R.W.L., 1989. A Classification of igneous rocks and glossary of terms: re-commendations of the International Union of Geological Sciences Subcommission on the Systematics of Igneous Rocks. Blackwell.
Martin, H., 1986. Effect of steeper Archean geothermal gradient on geochemistry of subduction-zone magmas. Geology 14, 753–756.
Martin, H., Smithies, R.H., Rapp, R., Moyen, J.F., Champion, D., 2005. An overview of adakite, tonalite–trondhjemite–granodiorite (TTG), and sanukitoid: relationships and some implications for crustal evolution. Lithos 79, 1–24.
Maury, R.C., Sajona, F.G., Pubellier, M., Bellon, H., Defant, M.J., 1996. Melting of oceanic crust in young subduction/collision zones: the case of Mindanao (Philippines). Bull. Soc. Geol. Fr. 167, 579–595.
Mccarthy, T.C., Patiño Douce, A.E., 1997. Experimental evidence for high-temperature felsic melts formed during basaltic intrusion of the deep crust. Geology 25, 463–466.
Nandedkar, R.H., Ulmer, P., Müntener, O., 2014. Fractional crystallization of primitive, hydrous arc magmas: an experimental study at 0.7 GPa. Contrib. Miner. Petrol. 167, 1015.
Niu, Y., 2013. Global Tectonics and Geodynamics: A Petrological and Geochemical Approach. Science Press.
Peacock, S.M., Rushmer, T., Thompson, A.B., 1994. Partial melting of subducting oceanic

crust. Earth Planet. Sci. Lett. 121, 227–244.
Qi, L., Jing, H., Gregoire, D.C., 2000. Determination of trace elements in granites by inductively coupled plasma mass spectrometry. Talanta 51, 507.
Qian, Q., Hermann, J.R., 2013. Partial melting of lower crust at 10–15 kbar:constraints on adakite and TTG formation. Contrib. Miner. Petrol. 165, 1195–1224.
Rapp, R.P., Watson, E.B., 1995. Dehydration melting of metabasalt at 8–32 kbar: implications for continental growth and crust-mantle recycling. J. Petrol. 36, 891–931.
Rapp, R.P., Watson, E.B., Miller, C.F., 1991. Partial melting of amphibolite/eclogite and the origin of Archean trondhjemites and tonalites. Precambr. Res. 51, 1–25.
Ravna, E.K., 2000. Distribution of Fe 2q and Mg between coexisting garnet and hornblende in synthetic and natural systems: an empirical calibration of the garnet – hornblende Fe – Mg geothermometer. Lithos 53, 265–277.
Rushmer, T., 1991. Partial melting of two amphibolites: contrasting experimental results under fluid-absent conditions. Contrib. Miner. Petrol. 107, 41–59.
Sen, C., Dunn, T., 1994. Dehydration melting of a basaltic composition amphibolite at 1.5 and 2.0 GPa: implications for the origin of adakites. Contrib. Miner. Petrol. 117, 394–409.
Sisson, T.W., Ratajeski, K., Hankins, W.B., Glazner, A.F., 2005. Voluminous granitic magmas from common basaltic sources. Contrib. Miner. Petrol. 148, 635–661.
Su, Y., 2007. Geochronological and Geochemical Study on the A-type Granites from Junggar, Xinjiang, Graduate School of Chinese Academy of Sciences.
Sun, S.S., Mcdonough, W.F., 1989. Chemical and isotopic systematics of oceanic basalts: implications for mantle composition and processes. Geol. Soc. London Special Publ. 42, 313–345.
Takahahshi, E., Nakajima, K., Wright, T.L., 1998. Origin of the Columbia River basalts: melting model of a heterogeneous plume head. Earth Planet. Sci. Lett. 162, 63–80.
Tang, H., Zhao, Z., Huang, R., Han, Y., Su, Y., 2008. Primary Hf isotopic study on zircons from the A-type granites in eastern Junggar of Xinjiang, Northwest China. Acta Mineral. Sin. 28, 335–342.
Taylor, S.R., Mclennan, S.M., 1995. The geochemical evolution of the continental crust. Rev. Geophys. 33, 293–301.
Tera, F., Brown, L., Morris, J., Sacks, I.S., Klein, J., Middleton, R., 1986. Sediment incorporation in island-arc magmas: Inferences from 10 Be. Geochim. Cosmochim. Acta 50, 535–550.
Tian, J., Qunan, L., Guangming, F., Xiaomei, N., Chaobin, H., Fuming, W., Shuai, C., Weiwei, W., 2016. Mantle underplated pluton and stitching granite pluton from south side of the Karamaili fault in eastern Junggar: Geochronological, geochemical and Sr Nd isotopic constraints on their petrogenesis and tectonic implications. Acta Petrol. Sin. 32, 1715–1730.
Tingle, T.N., Jr., Green, H.W., Young, T.E., Koczynski, T.A., 1993. Improvements to Griggs-type apparatus for mechanical testing at high pressures and temperatures. Pure Appl. Geophys. 141, 523–543.
Wang, M., Tang, H., 2013. Reaction experiments between tonalitic melt and mantle olivine and their implications for genesis of high-Mg andesites within cratons. Sci. China Earth Sci. 56, 1918–1925.
Wang, M., Zang, C., Tang, H., 2019. The effect of P-T on the reaction between tonalitic melt and mantle lherzolite at 2–4 GPa and implications for evolution of North China Cratonic Lithosphere and generation of High Mg# andesite. Lithos 324, 626–639.
Xiong, X., Adam, J., Niu, H., Jinhua, W.U., Cai, Z., 2006. Trace element characteristics of partial melts produced by melting of metabasalts at high pressures: constraints on the formation condition of adakitic melts. Sci. China: Earth Sci. 49, 915–925.
Xiong, X.L., Adam, J., Green, T.H., 2005. Rutile stability and rutile/melt HFSE partitioning during partial melting of hydrous basalt: Implications for TTG genesis. Chem. Geol. 218, 339–359.
Xue, Y.G., Yong-Jun, L., Guo-Hui, Si, Hong-En, W., Yongzhi, Z., 2010. LA-ICP-MS Zircon U-Pb Dating of Kubusunan Granodiorite and the Enclaves from Kalamaili Area in Eastern Junggar, Xinjiang, and its geological implications. Earth Sci. – J. China Univ. Geosci. 35, 597–610.
Yan, C.X., Yang, G.X., Yong-Jun, L.I., Hong-En, W.U., Si, G.H., Zhang, Y.Z., 2008. Petrochemistry feature and tectonic significance of the kubusunan granitic rock mass in east junggar, xinjiang. Xinjiang Geol. 26, 220–224.
Yang, G., Li, Y., Wu, H., Zhong, X., Yang, B., Yan, C., Yan, J., Si, G., 2011. Geochronological and geochemical constrains on petrogenesis of the Huangyangshan A-type granite from the East Junggar, Xinjiang, NW China. J. Asian Earth Sci. 40, 722–736.
Yaxley, G.M., Green, D.H., 1998. Reactions between eclogite and peridotite: Mantle refertilisation by subduction of oceanic crust. Schweiz. Mineral. Petrogr. Mitt. 78, 243–255.
Zheng, Y.F., Chen, Y.X., Dai, L.Q., Zhao, Z.F., 2015. Developing plate tectonics theory from oceanic subduction zones to collisional orogens. Sci. China: Earth Sci. 58, 1045–1069.
Zhu, X., Wang, Z., Wang, Y., Bi, H., 2006. Geological character of post-orogenic alkaline granites in Xinjiang. Acta Petrol. Sin. 22, 2945–2956.